Instability-induced pattern generation in architectured materials — A review of methods

Rachel Azulay [a,*], Christelle Combescure [b,c], Justin Dirrenberger [a]

[a] Laboratoire PIMM, Arts et Metiers, CNRS, Cnam, HESAM Université, 75013 Paris, France
[b] Univ. Bretagne Sud, UMR CNRS 6027, IRDL, F-56100 Lorient, France
[c] Saint-Cyr Coëtquidan Military Academy, CReC Saint-Cyr, 56381 Guer Cedex, France

ARTICLE INFO

Keywords:
Stability analysis
Buckling
Architectured materials
Pattern generation
Bifurcation

ABSTRACT

Architectured materials exhibit unconventional properties directly linked to their geometry. When composed of slender elements, architectured materials can undergo large deformations exhibiting geometric non-linearities through buckling or snapping behaviours of the cell walls. This can create a new pattern in the material with different properties than the original structure. In this article, we present a review of methods for studying pattern generating architectured materials caused by elastic instabilities. We start by reviewing the relevant studies on a classical example : hexagonal honeycombs under compression. We highlight their importance in identifying the underlying bifurcation phenomenon and their contributions to the elaboration of methods for studying mesoscopic (unit-cell length) pattern changes in architectured materials. We then exhaustively review the methods and tools used up to now to study the post-bifurcated behaviour of such materials subject to elastic instabilities.

1. Introduction

Challenges faced by modern engineering have pushed the limits of materials science and called for a new class of material to be created: architectured materials. These materials, sometimes called architected or even hybrid materials, were conceived to fulfill the increasingly demanding requirements of engineering applications when conventional bulk materials could not be used (Ashby and Bréchet, 2003; Bouaziz et al., 2008; Barthelat, 2015; Estrin et al., 2019). Over the past decades, their development has been a growing field of interest (cf. Fig. 1), especially due to the improvement and recent breakthroughs in additive manufacturing (Schaedler and Carter, 2016; Frenzel et al., 2017; Surjadi et al., 2019; Maconachie et al., 2019; Kadic et al., 2019; Spiegel et al., 2020; Mayer et al., 2020; Feenstra et al., 2021; du Plessis et al., 2021; Christensen et al., 2015). They are constructed from carefully chosen materials with a specific geometry, topology and morphology. By precisely controlling these parameters, new unprecedented properties mainly related to the architecture of the material can be created or enhanced, expanding the material-property space. As a consequence, previously correlated material properties such as strength and density can be separated and tailored for the required application.

It is commonly accepted to identify three scales in architectured materials (Brechet and Embury, 2013; Barthelat, 2015; Poncelet et al., 2018): the microscopic scale, describing the constitutive material's (or materials') microstructure; the macroscopic scale, describing the architectured material as a whole; and the mesoscopic scale describing the constitutive material's (or materials') arrangement in space, i.e. the architecture. **The specificity of architectured materials is that their novel properties mainly arise from its mesoscopic architecture** as opposed to conventional materials where it arises from their microstructure (Gibson and Ashby, 1982; Ashby and Bréchet, 2003; Bouaziz et al., 2008; Dunlop et al., 2011; Barthelat, 2015; Bertoldi, 2017; Viard et al., 2020; Wang et al., 2023). The scale separation in conventional and architectured materials is illustrated Fig. 2. Therefore, in architectured materials, the mesoscopic architecture can be adjusted to change the macroscopic material properties to suit a particular application.

The development of metamaterials – which refer in this article to architectured materials for photonic and phononic crystals (Lu et al., 2009; Pennec et al., 2010), wave guides and noise reducing structures – has resulted in transferable concepts for the design of the mesoscopic architecture. More specifically the distinction made between passive metamaterials, which have unchanged bulk properties when subject to external stimuli, and active metamaterials, which undergo changes to molecular arrangements, material phase or crystal microstructure caused by external stimuli (Shaw and Hopkins, 2015; Pishvar and

* Corresponding author.
E-mail address: rachel.j.azulay@gmail.com (R. Azulay).

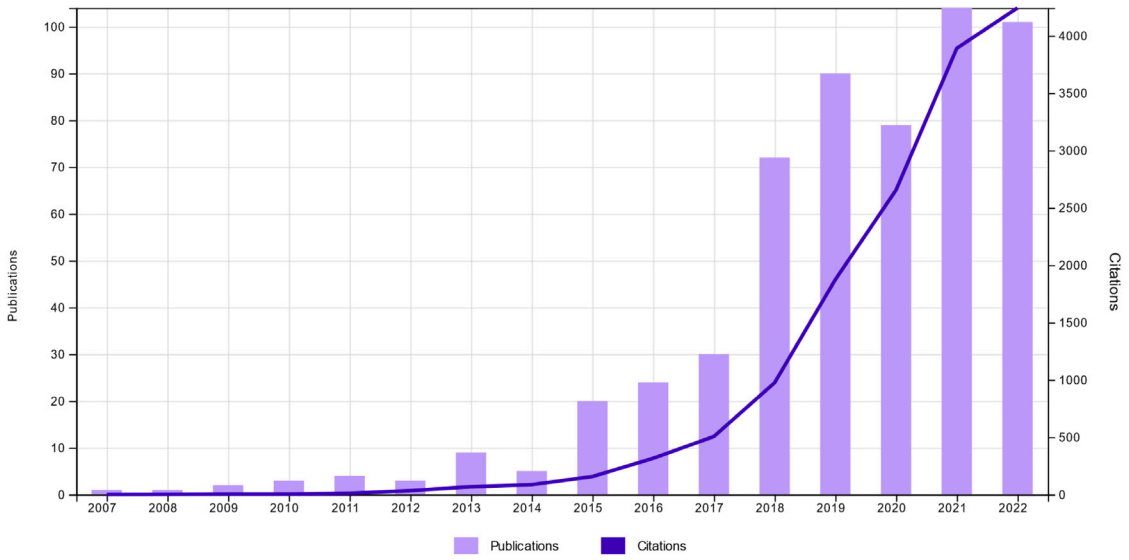

Fig. 1. Number of publications and citations containing "architectured materials" or "architected materials" from 2007 to 2022. *Source:* Data from Web of Science.

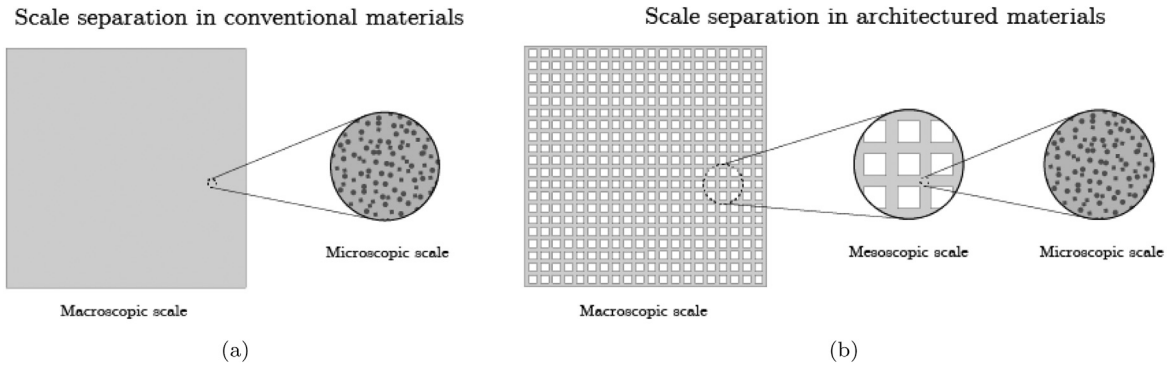

Fig. 2. Difference in scale separation in conventional materials and architectured materials. (a) In conventional materials, there are two distinct scales: the macroscopic scale and the microscopic scale, (b) In architectured materials, there are three distinct scales: like in classical materials there are macroscopic and microscopic scales but a third, intermediate "mesoscopic" scale exists of the order of the material's cell size.

Harne, 2020) have inspired the design of shape-reconfigurable architectured materials. For example, when composed of slender elements, architectured materials can undergo large deformations exhibiting geometric non-linearities through buckling or snapping behaviours of the mesostructure (Bertoldi et al., 2017). Other mechanisms, out of the scope of this article, such as origami and kirigami (Bertoldi et al., 2017) can be used for shape-morphing architectured materials but they rely on kinematics, whereas elastic instabilities take into account mechanical notions such as force or internal stress. In a large majority of cases, buckling or snapping are considered failure phenomena to be avoided but it is not necessarily catastrophic as stable post-buckling behaviours can be attained. The first study to observe such mesoscopic (unit-cell) post-buckling in architectured materials was conducted by Papka and Kyriakides (1994). The authors noticed a new localised pattern, presented Fig. 3(a) caused by periodic buckling of the cell walls. The pattern was then stabilised in the material by Mullin et al. (2007) who observed uniform pattern transformations throughout the specimen generated by elastic instabilities for an elastomer composed of a square array of holes under compression (see Fig. 3(b)).

Later on, this phenomenon has been proved useful for controlling wave propagations as Bertoldi and Boyce (2008) demonstrated that mechanical deformation could be used to control the band structure of an elastomer composed of square arrays of circular holes and hexagonal arrays of circular holes. Shan et al. (2014) showed that for a honeycomb which exhibits three distinct patterns for three distinct boundary conditions, the wave propagation properties are entirely different, behaving like four distinct materials (one undeformed and three patterns). In both cases compressing the material removes certain band gaps, shifts others and create new ones which did not exist for the initial structure. To illustrate this phenomenon, the results from Shan et al. (2014) are presented Fig. 4. Furthermore, the study conducted by Shim et al. (2015) characterised the link between the change in material properties to the amount of deformation of the structure. Although this paragraph has expanded on phononic applications, other applications of patterning include modifying the material's Poisson ratio, effective negative swelling ratio or chirality (Bertoldi et al., 2017).

There exists multiple control strategies for triggering shape-reconfiguration in architectured materials. Mechanical loading is the most commonly found stimuli in the literature (Li et al., 2021; Fang et al., 2018; Overvelde et al., 2017, 2016; Babaee et al., 2016; Chen et al., 2014; Yang et al., 2018; Shang et al., 2018; Blees et al., 2015; Song et al., 2015; Neville et al., 2016; Mullin et al., 2007; Bertoldi et al., 2008) but swelling has also been investigated and seems to be a promising approach for triggering pattern switches (Kang et al., 2013; Wei et al., 2020; Curatolo, 2018; Turcaud et al., 2011; Harrington et al., 2011; Guiducci et al., 2014, 2015, 2016; Le Duigou et al., 2019, 2021; Liu et al., 2016). Other, less common methods which include the use of magnetic fields (Danas et al., 2012; Psarra et al., 2017; Lefèvre et al., 2017; Liu et al., 2019; Psarra et al., 2019), temperature (Qu et al., 2017; Wang et al., 2016), electrochemical stimuli (Xia et al., 2019) and even

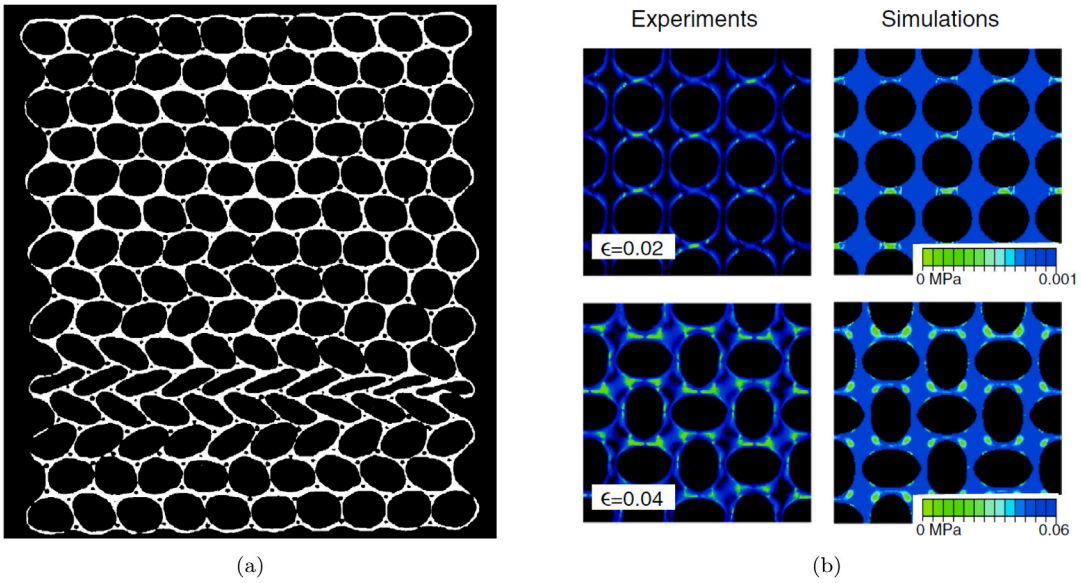

Fig. 3. Localisation and stabilisation of pattern formation (a) Localisation bands following localised pattern formations in polycarbonate circular-celled honeycomb, from Papka and Kyriakides (1999a); (b) Homogeneous pattern formation in an elastomeric specimen, from Mullin et al. (2007) .

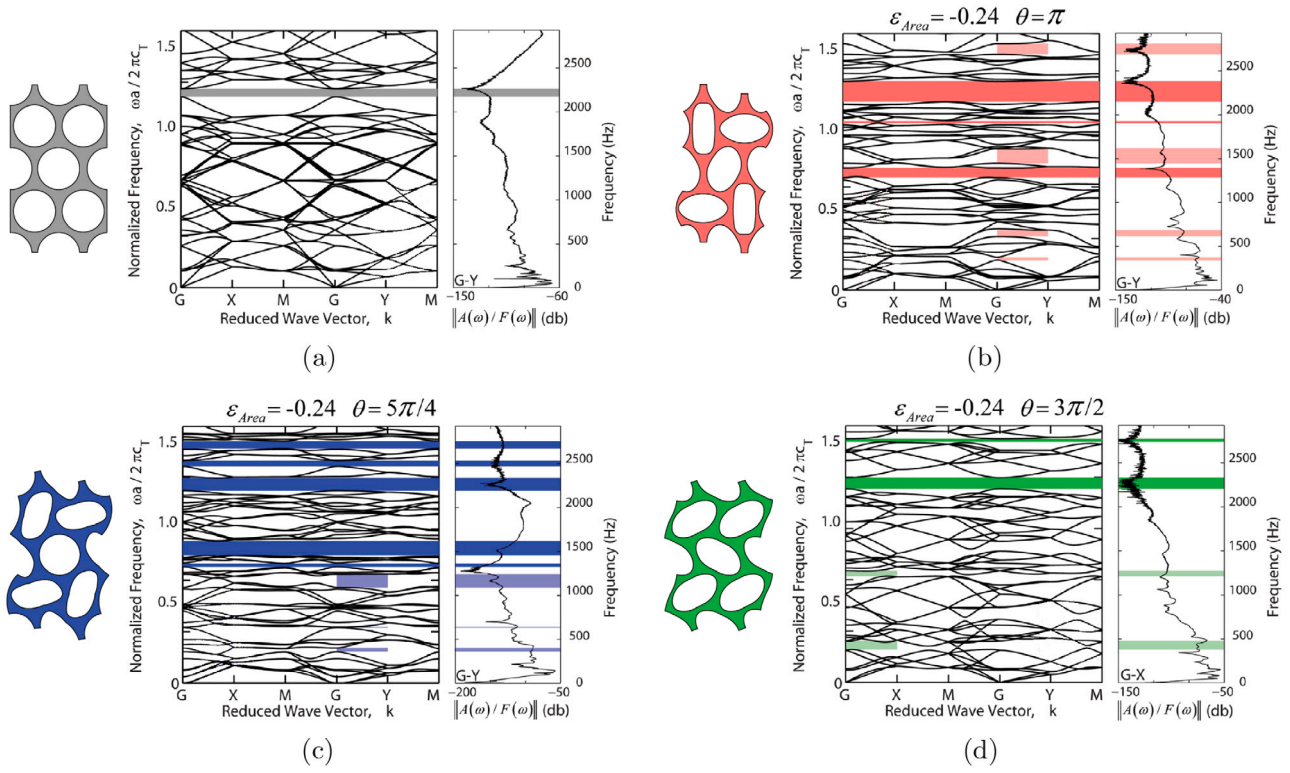

Fig. 4. Adapted from Shan et al. (2014) : For each mode, comparison between the numerical dispersion relations (left) and the experimental frequency response functions (right) of the system obtained for different values of the loading path angle θ. (a) Undeformed configuration; (b) Biaxial load; (c) Equibiaxial load; (d) Uniaxial mode.

actuation (Song et al., 2016; Shaw and Hopkins, 2015) have been successfully experimented. Additionally, a large number of experimental studies have proven that the geometric parameters of the mesostructure along with its constitutive material have a significant influence on the post-buckling behaviour of the architectured material (Overvelde et al., 2012; Hu et al., 2013; He et al., 2017; Gao et al., 2018; Combescure et al., 2016; Bertoldi and Boyce, 2008; He et al., 2018).

A major finding from the study of these types of architectured materials is that the new pattern may need more than the original unit cell to be described as buckling of the cell walls may occur at a larger wavelength than the initial geometric unit cell (Geymonat et al., 1993; Overvelde and Bertoldi, 2014; Hoyle, 2006). This creates additional difficulties that need to be taken into account when modelling architectured materials as thorough investigations, which must include a possible change in pattern periodicity, are necessary before modelling their behaviour under compression.

Instability-induced pattern generation in architectured materials involves complex mechanisms and is conditioned on a wide range of parameters. Consequently, this intricate behaviour has led to the

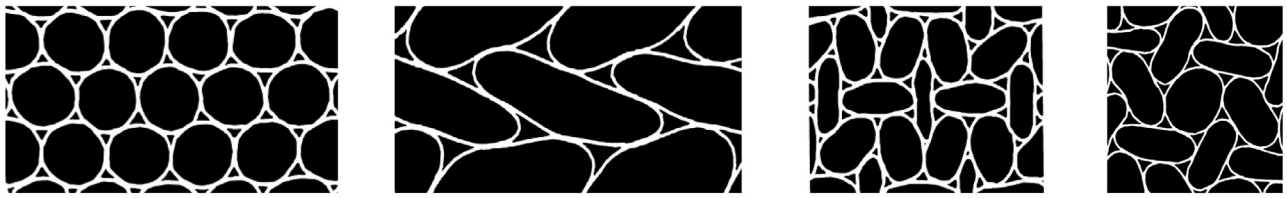

Fig. 5. Pattern changes for a hexagonal arrangement of circular holes. The x axis runs horizontally and the y axis vertically. (a) Undeformed configuration, (b) Uniaxial compressed vertically, (c) Biaxially compressed with a 1:3 ratio, (d) Equibiaxially compressed.
Source: Adapted from (Papka and Kyriakides, 1999a).

development of methods, all interdependent, for modelling the principal path, the bifurcation point and the post-bifurcated pattern. These specific and very effective models will be presented in detail in this review. In the first part of the article, we will present an extensively studied example of such materials, the honeycomb lattice, as studying this architecture has been the starting point of many theoretical and numerical approaches. In the second part, we will develop on the existing methods which model mesoscopic pattern generation in architectured materials.

2. Historic example: 2D hexagonal honeycombs under compression

Hexagonal honeycombs subject to in-plane crushing have been exhaustively studied for the past 40 years due to their wide variety of applications (Gibson and Ashby, 1982; Zhang et al., 2015). We present here a chronological review of the behaviour of these structures as each contribution has played a key role in understanding the mechanisms and setting the theories for studying architectured materials under compression. The regular honeycomb structure exhibits both distinct pattern changes for different loading conditions and a change in period after pattern transformation takes place.

Many studies on the in-plane compression of hexagonal honeycombs have been carried out since the 1980s (Gibson and Ashby, 1982; Guo and Gibson, 1999; Chung and Waas, 2002). Nevertheless, the first study to mechanically characterise and explain the in-plane compressive response of hexagonal honeycombs was conducted by Papka and Kyriakides (1994). Their experiments aimed to be as simple as possible to fully dissociate any biasing effects such as bi-axial loading, inertia or any three-dimensional effect which may alter their characterisation. They performed quasi-static compression tests on 9 rows by 6 columns aluminium hexagonal cell specimens under displacement control and obtained the well-known stress–strain curve for cellular solids (Gibson and Ashby, 1988). The observed behaviour is divided into three parts: first, the sample undergoes an initial high stiffness regime which the authors associated to a stable uniform elastic deformation in the specimen. Then a plateau stress regime appears where the material behaves as if it had zero stiffness. During this phase, both collapsed and uncollapsed cells coexist, and the collapse phenomenon propagates row by row until the final regime, when all the cells have collapsed and the response becomes stiff again, now due to densification. Coupled with numerical simulations, the authors established the connection between the existence of a bifurcation point on the principal loading path and the instant when the specimen begins to collapse.

The same authors (Papka and Kyriakides, 1998) conducted a second experiment, much like their first, for studying the uniaxial compression a hexagonal arrangement of 15 × 10 polycarbonate circular cells. This specific polymeric material was chosen to study the compressive response and crushing behaviour of a rate-dependent specimen. The results showed the same overall response as their previous study with three distinct regimes. It was found that the specimen required more compressive stress to trigger the initial instability when the displacement rate increased. Their experiments were coupled with full-scale numerical analyses which confirmed the method previously used in Papka and Kyriakides (1994) and proved the accuracy at which the behaviour of these materials can be predicted.

Having gained this insight, Papka and Kyriakides (1999a,b) went deeper into understanding the in-plane crushing of honeycombs by conducting a more extensive study to characterise their biaxial compressive behaviour. This time, the specimens were composed of a hexagonal arrangement of 18 × 21 polycarbonate circular cells. As they needed to test the response of their specimen under very large displacements, they custom built a testing device specifically designed for the biaxial compression of low density cellular materials. Their results confirmed their previous work concerning uniaxial compression. After testing multiple biaxial loads, three distinct patterns and mechanisms were identified: Mode I, a shear-like mode obtained when the specimen is compressed uniaxially, Mode II, which appears when biaxially compressed with a ratio of 3 and Mode III, a flower-like mode obtained for equibiaxial compression, cf Fig. 5.

The second part of the study consisted in a full-scale finite element analysis of the specimen under several biaxiality ratios. For the sake of calculation resources, they reduced the size of their numerical specimen but still obtained results in accordance with their experimental results. They concluded that the boundary condition imposed on the specimen influence the critical load necessary to attain the onset of instability but may not have an influence on the pattern generated when the instability is reached (Papka and Kyriakides, 1999a).

From these experiments, came the necessity of elaborating a method to determine the bifurcation point for cellular solids. Triantafyllidis and Schraad (1998) conducted a hybrid analytical and numerical analysis of the failure surfaces in aluminium honeycombs of infinite size. The authors tested their honeycomb for a specified ratio of principal stresses and certain load orientations in both finite and infinite media. The specimen being subject to a quasi-static compression, it satisfies the equations for static equilibrium and its behaviour is governed by them. As a result, the authors defined the bifurcation point as a loss of uniqueness for the solution, in the macroscopic stress–strain space, satisfying the equilibrium equations. In addition, the experiments conducted on the compression of hexagonal honeycombs showed that the patterns formed may occur on more cells than the initial unit cell. To take this into account and consider the appropriate unit cell for pattern transformation, the instabilities were investigated at both the macroscopic and mesoscopic scale by applying Bloch's Theorem at boundary nodes, as first proposed by Geymonat et al. (1993). The method is explained in detail in Section 4 which reviews all methods used for determining the post-bifurcated solutions of a structure.

For design purposes, researchers were interested in understanding and anticipating the patterns obtained for hexagonal honeycombs. The work by Ohno et al. (2002) numerically investigates the underlying mechanism for pattern generation in infinite specimens. The authors proposed a homogenisation framework and criterion for the infinite structure in order to determine the onset of bifurcation. For their analysis, they examined a 2 × 2 unit cell which corresponds to the mesoscopic pattern wavelength observed in experimental studies.

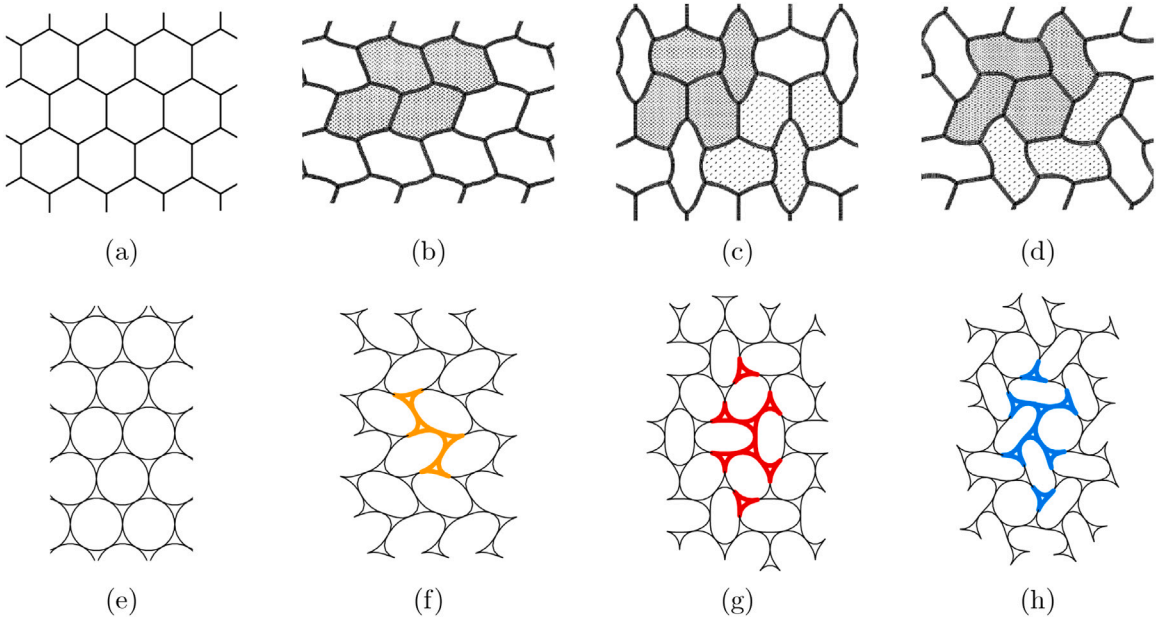

Fig. 6. (a) Undeformed hexagonal honeycomb, (b–d) Adapted from (Ohno et al., 2002): Identified modes for a hexagonal honeycomb under compression. (b) Mode I — uniaxial compression, (c) Mode II — Biaxial compression, (d) Mode III — Equibiaxial compression. (e–h) Adapted from (Combescure et al., 2020): Identified modes for a circular-celled honeycomb under compression. The coloured walls indicate the minimum number of cells necessary to describe the pattern. (e) Undeformed hexagonal honeycomb; (f) Mode I — uniaxial compression; (g) Mode II — Biaxial compression; (h) Mode III — Equibiaxial compression.

Multiple Cauchy stress compression ratios were numerically analysed and mesoscopic instabilities were found for all loading paths. They identified the bifurcation point as being a symmetric bifurcation point, i.e. typical pitchfork shaped bifurcation branch, explained by the high degree of symmetry in the structure. Their analysis concluded on the existence of three types of bifurcation points, one for each distinct pattern, which were all obtained numerically. Simple bifurcation points, where only one eigenvalue of the tangent stiffness matrix becomes zero at the critical load, exist when the compressive stress is transferred to only one direction of the cell walls. Double and triple bifurcation points, for which two or three eigenvalues of the tangent stiffness matrix simultaneously become zero at the critical load, exist when two directions of the cell walls are compressed. The authors also found that the pattern generated correspond to two or three linear combinations of the simple mode for double and triple bifurcation points respectively.

Continuing this work, Okumura et al. (2002) aimed to shed light on which mesoscopic buckling modes, or patterns, are experimentally observed. The authors performed macroscopic and mesoscopic stability analyses for stress and strain controlled of boundary conditions on the same 2×2 unit cells as in Ohno et al. (2002). The mode was considered stable if the unit cell internal energy was minimal compared to the other possible modes. They mapped the buckling modes under biaxial compression for macroscopic stress and strain control and found there were major differences for the two different boundary conditions, especially concerning the flower-mode. More specifically for Mode III, the authors find it to be mesoscopically stable for macroscopic strain control and unstable when controlling macroscopic stress. The authors conclude on the macroscopic stability of the specimen but the reasons for this seem to require further investigations according to Combescure et al. (2016).

The existence and stability of the three bifurcation modes were further investigated by Combescure et al. (2016). The authors performed a numerical analysis on the influence of the loading device on the stability of the infinite hexagonal honeycomb. In their work, they compared three stability criteria: Bloch Wave stability for mesoscopic stability, loss of rank-one convexity for macroscopic stability and a third *ad hoc* criterion which evaluates the positive definiteness of the second derivative of the structure's energy. In their article, the flower-mode is discussed more in detail than the other two, as previous conclusions concerning the stability of this pattern were not unanimous. To help solve the highly symmetric stability and post-buckling analysis, elements from group theory were used to reduce the solution space and guide the solver. With the help of Bloch wave analysis, Combescure et al. (2016) computed the bifurcation point and the post-buckling stability analysis for every mesoscopic wavelength under three types of boundary conditions: displacement control, dead load Biot stress control, and live load pressure control. For each of these configurations, the equilibrium equations are solved by a branch-following algorithm and the bifurcation point is identified as the instant the solution loses its uniqueness. Each bifurcation point is observed to break up the symmetry of the original structure by increasing the size of the pattern unit cell. Both Mode I and II present mesoscopic and macroscopic stability. Mode III was found mesoscopically stable under displacement controlled loads but macroscopically unstable for the infinite specimen. Their numerical analysis pinpointed the dependence of the macroscopic loading device on the stability of the bifurcated paths. In addition they explained the reason for experimentally observing mode III on finite-sized specimens. The authors found the mode to be stable for large finite wavelengths, in particular for the wavelengths corresponding to the size of the experimental specimen. Furthermore, it was found that the *ad hoc* stability criterion is insufficient to conclude on the stability of the structure.

Until recently, most theoretical analyses were performed on hexagonal honeycombs but very few on hexagonal arrangements of circular-celled honeycombs. Combescure et al. (2020) decided to analyse the stability and post-buckling analysis of circular cell honeycombs for both square and hexagonal arrangements. The infinite-sized specimen was loaded parallel or at an angle to the axes of orthotropy for different constituting materials of the cell walls. For their analysis, the same theories and methods employed in Combescure et al. (2016) were used and they observed identical behaviour for the hexagonal matrix of circular cells and hexagonal cells, shown Fig. 6. The authors also found that for square arrangements, the bifurcated mode is never macroscopically stable therefore never creates any pattern.

Other buckling pattern, distinct from the three modes presented before, have been experimentally observed for surface-attached honeycomb structures (Kang et al., 2013). By binding the cellular structure to

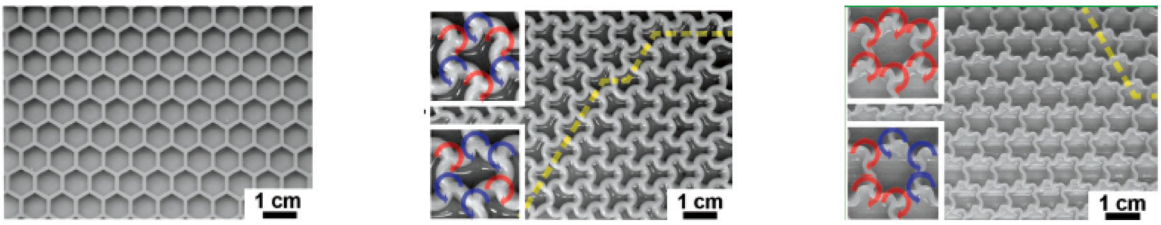

Fig. 7. Buckling-induced reversible pattern formation in a supported macroscale honeycomb lattice. The ratio length over the height of a wall l/h of the honeycomb struts is modified between (b) and (c) to obtain different buckled patterns (a) Undeformed honeycomb (b) Achiral buckled configuration ($l/h = 2$) (c) Chiral configuration ($l/h = 3.17$). *Source:* Adapted from Kang et al. (2013).

a rigid substrate, the authors numerically and experimentally showed that a higher buckling mode could be reached. In their experiments, they tuned the modes by changing the thickness over length ratio (t/l) and the length over the height of a wall (l/h), also called aspect ratio of the plate. Even if they used swelling to experimentally trigger the instabilities, they also specified that mode could be reached under in-plane compressive loads. This finding is particularly interesting as the patterns reached by the authors preserves the translational symmetry of the structure, unlike the previously discussed modes (see Fig. 7).

Studying hexagonal honeycombs under in-plane compressive loads has been the prelude to many, more general methods for studying periodic architectured materials due to the complex behaviours it is able to exhibit simultaneously: multiple buckling modes, change in periodicity and stability of its buckled configurations. In the following section, we will review the methods used for modelling elastic buckling in periodic architectured materials. We highlight that even if the methods were employed on a 2D architecture, they are not limited to this and are also valid for 3D architectured materials.

3. Modelling elastic buckling in architectured materials

Modelling pattern generating mechanical structures is not limited to the field of architectured materials. Of the wide range of systems which exhibit such buckling behaviour, all have in common that their special feature can be explained by bifurcation theory. In this section, we will first present concepts and methods relative to bifurcation theory and its connection to the study of shape-morphing architectured-materials. Then, we will present numerical methods for predicting the material's behaviour and the creation of bifurcation modes.

Throughout this article, scalars, vectors and tensors will be respectively denoted by A, $\mathbf{B}$ and $\underline{\mathbf{C}}$. Time derivatives will be written $\dot{\mathbf{x}}$.

3.1. Equilibrium and stability

Compressing architectured materials appears to be an initially homogeneous deformation which, at a certain critical point, becomes heterogeneous and a regular deformation pattern emerges. This is a perfect illustration of a phenomenon which is explained by bifurcation theory. At a critical load level, the solution the system's governing equations ceases to be unique and stable, creating a bifurcation point on the "principal" loading path. This generates drastic changes in the system, generating alternative, "bifurcated" deformation patterns (Bigoni, 2012) as observed experimentally in hexagonal honeycomb structures.

Bifurcation and stability analyses are closely related, especially concerning engineering applications. Therefore bifurcated solutions will only be physically observed if the bifurcated path is stable. In the following paragraphs, we present the general theory for determining bifurcation points and stable bifurcation paths for quasi-static compression.

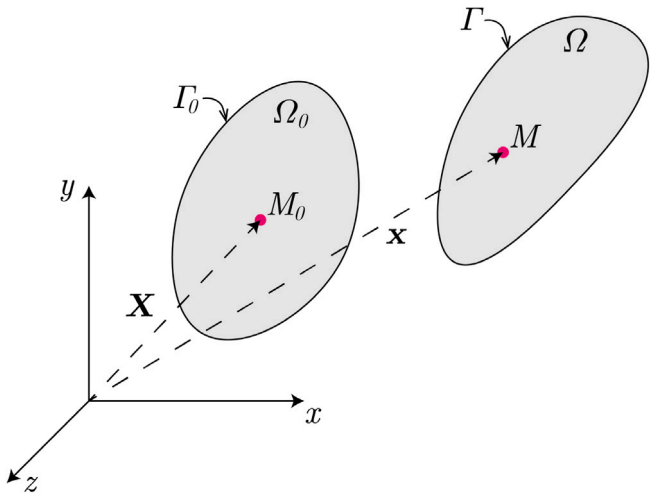

Fig. 8. Illustration of the system's configurations. M is a point in the elastic body $\mathcal{B}$.

3.1.1. Equilibrium configurations

The first step for finding bifurcation points is to calculate the principal equilibrium path. For solving the system's governing equations, a hypothesis concerning the initial conditions needs to be formulated. Therefore, we suppose the equilibrium equation to be unique and stable in some neighbourhood of the initial stress-free configuration.

Two equivalent methods exist for finding equilibrium configurations: the principle of virtual power applied in Bertoldi et al. (2008) and the principle of total potential energy used by Combescure et al. (2016). We will present both, which are completely equivalent.

First we consider an elastic body $\mathcal{B}$ occupying the region Ω with surface area Γ. We define the reference coordinates of the initial undeformed configuration Ω_0 as $\mathbf{X}$, and the current coordinates $\mathbf{x}(\mathbf{X}, \mathbf{t})$ at any time t using Lagrangian formulation (cf. Fig. 8).

The deformation gradient is given by:

$$\begin{aligned} \underline{\mathbf{F}}(\mathbf{X}, t) &= \frac{\partial \mathbf{x}}{\partial \mathbf{X}} \\ F_{ij} &= \frac{\partial x_i}{\partial X_j}, \quad (i, j) \in N \times N \end{aligned} \tag{1}$$

And $J = det(\mathbf{F})$.

The displacement $\mathbf{u}$ is defined by:

$$\mathbf{u}(\mathbf{X}, t) = \mathbf{x}(\mathbf{X}, t) - \mathbf{X} \tag{2}$$

The Cauchy stress tensor $\underline{\boldsymbol{\sigma}}$ is defined by:

$$\underline{\boldsymbol{\sigma}} \cdot \mathbf{n} d\Gamma = \mathbf{t} d\Gamma \tag{3}$$

With $\mathbf{n}$ the unit normal vector to a surface element $d\Gamma$ in the current configuration and $\mathbf{t}$ the vectorial stress on a plane of normal $\mathbf{n}$.

Nanson's formula ties $\mathbf{n}$ the unit normal to a surface element $d\Gamma$ in the current configuration to $\mathbf{N}$ the unit normal to a surface element $d\Gamma_0$ in the initial configuration:

$$\mathbf{n}d\Gamma = J\underline{\mathbf{F}}^{-T}\mathbf{N}d\Gamma_0 \tag{4}$$

With Γ_0 the initial surface of the undeformed body $\mathcal{B}$. By combining Eqs. (3) and (4), we obtain the first Piola–Kirchhoff stress tensor:

$$\underline{\mathbf{S}} = J\underline{\boldsymbol{\sigma}}\underline{\mathbf{F}}^{-T} \tag{5}$$

Principle of virtual power

From the definitions presented above, we state the principal of virtual power which defines the equilibrium configuration of our system. In full Lagrangian description we have:

$$-\int_{\Omega_0} \underline{\mathbf{S}} : \dot{\underline{\mathbf{F}}}\, d\Omega_0 + \left[\int_{\Omega_0} J\mathbf{f}\cdot\dot{\mathbf{x}}\, d\Omega_0 + \oint_{\Gamma_0} \frac{d\Gamma}{d\Gamma_0}\mathbf{t}\cdot\dot{\mathbf{x}}\, d\Gamma_0\right] = 0 \tag{6}$$

The principle provides the Lagrangian form of equilibrium:

$$div(\underline{\mathbf{S}}) + J\mathbf{f} = 0 \tag{7}$$

with $\mathbf{f}$ the body forces acting on Ω.

Principle of minimum total potential energy

The principle of minimum total potential energy states that if a body is in equilibrium, the admissible displacement field $\mathbf{u_0}$ which minimises the total potential energy $\mathcal{E}$ of all admissible displacement fields $\mathbf{u}$ corresponds to the equilibrium solution. Therefore, the equilibrium configurations are found by setting to zero the first derivative of the total potential energy $\mathcal{E}$ with respect to the displacement $\mathbf{u}$. Such first derivative written $\mathcal{E}_{,\mathbf{u}}$ is a linear operator on $\mathbb{R}^N$, N the total number of degrees of freedom of the structure. Such a derivative is the "Frechet derivative" defined by:

$$\lim_{\|\delta\mathbf{u}\|\to 0} \frac{\mathcal{E}(\mathbf{u}+\delta\mathbf{u}) - \mathcal{E}(\mathbf{u}) - \mathcal{E}_{,\mathbf{u}}\,\delta\mathbf{u}}{\|\delta\mathbf{u}\|} = 0 \tag{8}$$

$\delta\mathbf{u}$ can be fixed in $\mathbb{R}^N$ such that $\delta\mathbf{u} = \epsilon\mathbf{d}$ with $\mathbf{d}$ a unit vector and $\epsilon \to 0$. Eq. (8) becomes:

$$\mathcal{E}_{,\mathbf{u}}\,\mathbf{d} = \left[\frac{\partial\mathcal{E}(\mathbf{u}+\epsilon\mathbf{d})}{\partial\epsilon}\right]_{\epsilon=0} \tag{9}$$

The system is therefore at an equilibrium when:

$$\mathcal{E}_{,\mathbf{u}}\,\delta\mathbf{u} = 0, \quad \forall\mathbf{u}\in\mathbb{R}^N \tag{10}$$

The total potential energy of a body is the sum of the strain energy stored in the body ($\mathcal{U}$) and ($\mathcal{V}$) the work done by external forces.

$$\mathcal{E} = \mathcal{U} + \mathcal{V} \tag{11}$$

The strain energy stored in the body ($\mathcal{U}$) is established using strain energy density functions (W).

$$\mathcal{U} = \int_{\Omega} W(\underline{\mathbf{F}})\, d\Omega \tag{12}$$

For small strains the energy density function is well established, but for large strains and large deformations the density functions depend on the choice of the constitutive material's behaviour model.

The following equation gives the total work done by applied body force $\mathbf{f}$ and surface force $\mathbf{t}$.

$$\mathcal{V} = -\left[\int_{\Omega}\mathbf{f}\cdot\mathbf{u}\, d\mathbf{x} + \oint_{\Gamma}\mathbf{t}\cdot\mathbf{u}\, d\Gamma\right] \tag{13}$$

Therefore:

$$\mathcal{E} = \int_{\Omega} W(\underline{\mathbf{F}})\, d\Omega - \left[\int_{\Omega}\mathbf{f}\cdot\mathbf{u}\, d\mathbf{x} + \oint_{\Gamma}\mathbf{t}\cdot\mathbf{u}\, d\Gamma\right] \tag{14}$$

As a result, the equilibrium configurations satisfy:

$$\mathcal{E}_{,\mathbf{u}}\,\mathbf{d} = \int_{\Omega} W_{,\mathbf{u}}(\underline{\mathbf{F}})\,\mathbf{d}\, d\Omega - \left[\int_{\Omega}\mathbf{f}\,\mathbf{d}\, d\mathbf{x} + \oint_{\Gamma}\mathbf{t}\,\mathbf{d}\, d\Gamma\right] = 0 \tag{15}$$

The equilibrium configuration helps identify critical points, defined as the instant the equilibrium solution loses its uniqueness. Critical points are classified into two categories: limit load points and bifurcation points, as depicted Fig. 9.

3.1.2. Stability of an equilibrium path

After defining the equilibrium criterion, we are now interested in assessing the stability of bifurcated paths.

Architectured materials are considered as conservative systems with finite degrees of freedom. Therefore, the stability criterion to satisfy is the one stated by Lejeune-Dirichlet (Rouche et al., 1977). Considering the system described by the equilibrium equations presented above, the system is necessarily and sufficiently stable in an equilibrium state $\mathbf{u_e}$ if:

$$\left[(\mathcal{E}_{,\mathbf{uu}}\,\delta\mathbf{u})\delta\mathbf{u}\right]_{\mathbf{u}=\mathbf{u}_e} > 0 \tag{16}$$

With $\mathcal{E}_{,\mathbf{uu}}$ a bilinear operator defined similarly to Eq. (9), $\mathbf{d}, \mathbf{h}$ unit vectors of $\mathbb{R}^N$ and $\epsilon, \kappa \in \mathbb{R}$:

$$(\mathcal{E}_{,\mathbf{uu}}\,\mathbf{d})\mathbf{h} = \left[\frac{\partial^2\mathcal{E}(\mathbf{u}+\epsilon\mathbf{d}+\kappa\mathbf{h})}{\partial\epsilon\partial\kappa}\right]_{\epsilon=\kappa=0} \tag{17}$$

3.2. Full-scale simulations and finite element analysis

For studying architectured materials, part of the community has been relying on full field finite element analyses to capture the instability observed in experimental results. We present here the formulation of instabilities in finite element analysis and the methods used for buckling and post-buckling analyses.

3.2.1. Finite element formulation of instabilities

Computing instabilities and its non-linear effects is a key aspect of structural analysis. The existence of simultaneous solutions after the onset of instability has required specific algorithms to be implemented which detect both bifurcation points and limit points. We present here the finite element considerations for the specific field of architectured materials. The results are of use in static analyses and solely in the elastic domain of the constitutive material.

For discrete systems under single parameter loads, the equilibrium state is described by:

$$\underline{\mathbf{K}}_T\,\Delta\mathbf{U} = \Delta\lambda\,\mathbf{P} \tag{18}$$

where $\underline{\mathbf{K}}_T$ the system tangent stiffness matrix, $\mathbf{P}$ the loading vector and $\Delta\mathbf{U}$, $\Delta\lambda$ are the displacement vector increment and proportional loading scalar increment, respectively.

Unstable behaviour can either be caused by the simultaneous existence of multiple equilibrium solutions for a given load, or a general loss of stiffness in the structure when loaded. In finite element formulation for hyperelastic materials, the computation of critical or instability points is analogous to finding the instant the tangent stiffness matrix becomes singular. The finite element formulation for Eq. (10) is equivalent to the criterion: $det(\underline{\mathbf{K}}_T) > 0$.

This corresponds to a positive definite tangent matrix $\underline{\mathbf{K}}_T$. The general method for checking on the positive definiteness of this matrix is achieved by either computing its determinant and assessing its sign or checking a change of sign in the diagonal elements of the diagonalised matrix (Wriggers, 2008). The stability condition on the determinant of the tangent matrix can be re-written by studying the standard eigenvalue problem:

$$\left(\underline{\mathbf{K}}_T - \alpha_i\underline{\mathbf{I}}\right)\boldsymbol{\omega}_i = \mathbf{0} \tag{19}$$

With

$$det(\underline{\mathbf{K}}_T) = \prod_{i=1}^{ndof}\alpha_i \tag{20}$$

where α_i are the eigenvalues and $\underline{\omega}_i$ the eigenvectors of $\underline{\mathbf{K}}_T$.

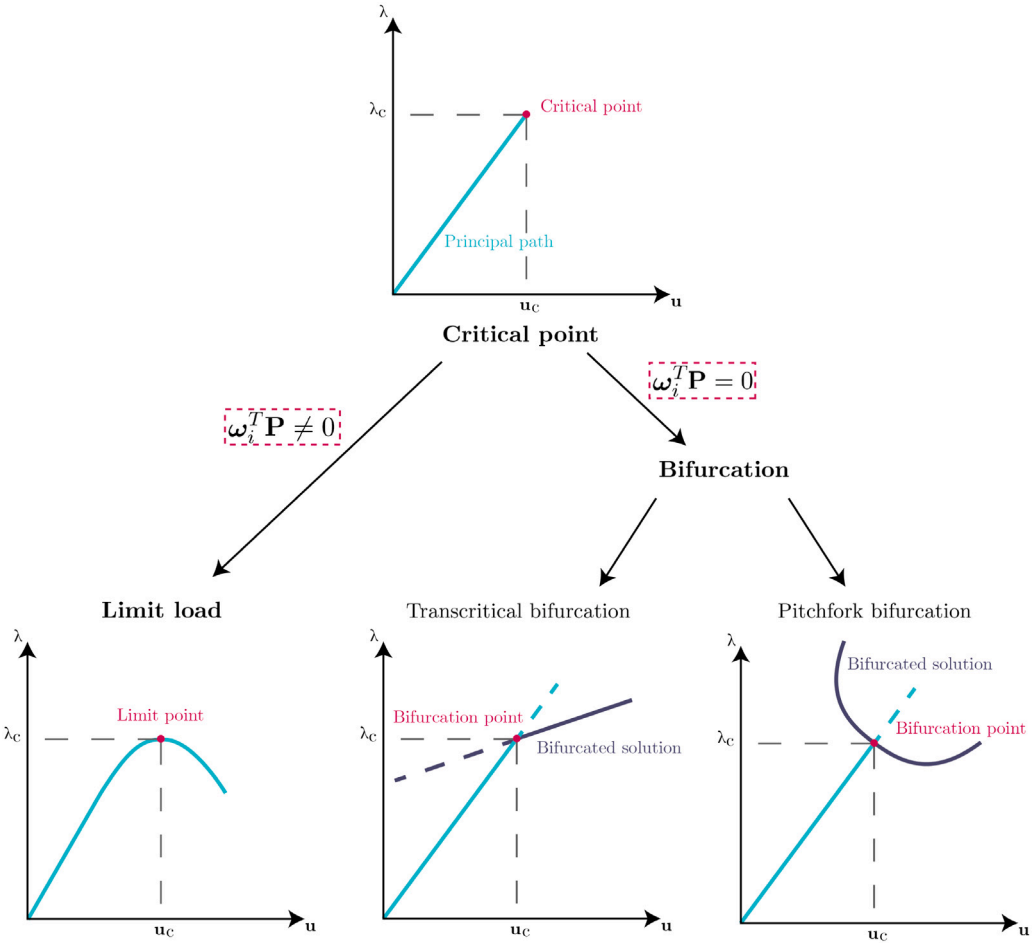

Fig. 9. Schematic representations of critical points.

We point out that in conservative systems, the tangent matrix is symmetric (Bufler, 1993). Hence, using the spectral decomposition the tangent matrix can be decomposed as follows: $\underline{\mathbf{K}}_T = \underline{\mathbf{W}}\,\underline{\mathbf{D}}_\alpha\,\underline{\mathbf{W}}^T$, where $\underline{\mathbf{W}}$ is the orthogonal matrix composed of the eigenvectors $\boldsymbol{\omega}_i$ of $\underline{\mathbf{K}}_T$ and $\underline{\mathbf{D}}_\alpha$, the diagonal matrix of eigenvalues α_i.

As stated in Section 3.1, the previous criterion identifies two types of instabilities: limit load points, and bifurcation points. The distinction between both types of instabilities is made by computing the eigenvectors associated with the eigenvalue analysis. From the eigenvalue analysis computed in Eq. (19) the instability points are defined as follows and illustrated Fig. 9:

$$\boldsymbol{\omega}_i^T \mathbf{P} \begin{cases} = 0 & \text{if bifurcation point} \\ \neq 0 & \text{if limit point} \end{cases} \tag{21}$$

Additionally, when dealing with highly symmetric systems such as honeycombs, as discussed in Section 3, bifurcation points can be multiple, meaning that more than one eigenvalue becomes null for the same loading parameter. Assessing the sign of the determinant, in this case, can lead to missing a bifurcation point since the determinant will not change its sign when an even number of eigenvalues change sign simultaneously. It is therefore highly recommended, when working with such symmetric systems, to work with a criterion based on the sign of individual eigenvalues rather than with the sign of the determinant.

3.2.2. *Buckling and post-buckling analyses*

Buckling in architectured materials can be predicted in finite element analysis by performing buckling analyses. This function is available in most finite element (FE) software to estimate the critical buckling load and associated buckled geometry of the structure. In most engineering applications, a linear buckling analysis is sufficient to check design requirements, but if a more complex problem involving material non-linearity, multiple simultaneous buckling modes or an unstable post-buckling response arises, a more complex non-linear buckling analysis is necessary (Ellobody, 2014). In this section, we present the general framework used by most FE codes for computing the analysis, which corresponds to solving an eigenvalue problem for the stiffness matrix.

The eigenvalue problem is obtained by splitting the tangent stiffness matrix into three distinct parts:

$$\underline{\mathbf{K}}_T = \underline{\mathbf{K}}_L + \underline{\mathbf{K}}_0 + \underline{\mathbf{K}}_\sigma \tag{22}$$

With $\underline{\mathbf{K}}_0$ the part of the stiffness matrix related to the initial deformations, $\underline{\mathbf{K}}_L$ the linear stiffness matrix and $\underline{\mathbf{K}}_\sigma$ the stress stiffness matrix comprising geometric non-linearity effects.

As specified in the previous paragraph, the structure is stable only if the stiffness matrix $\underline{\mathbf{K}}_T$ is positive definite. Therefore, the onset of instabilities is computed by searching for the loads when $\underline{\mathbf{K}}_T$ is singular. The problem becomes finding non-trivial incremental displacement vectors $\Delta\mathbf{U}$ (Waszczyszyn et al., 2013; Reddy, 2014) solutions to:

$$\underline{\mathbf{K}}_T\ \Delta\mathbf{U} = \mathbf{0} \tag{23}$$

A linear buckling analysis supposes that the displacement and stress states are completely independent close to the instability point. It often the case for beam and shell structures where the unstable behaviour does not depend on the membrane states (Wriggers, 2008). Therefore Eq. (22) is transformed into the following eigenvalue problem (Waszczyszyn, 1983; Nagy, 1979):

$$\left[\underline{\mathbf{K}}_L + \lambda\left(\underline{\mathbf{K}}_0 + \underline{\mathbf{K}}_\sigma\right)\right]\boldsymbol{\Phi} = \mathbf{0} \tag{24}$$

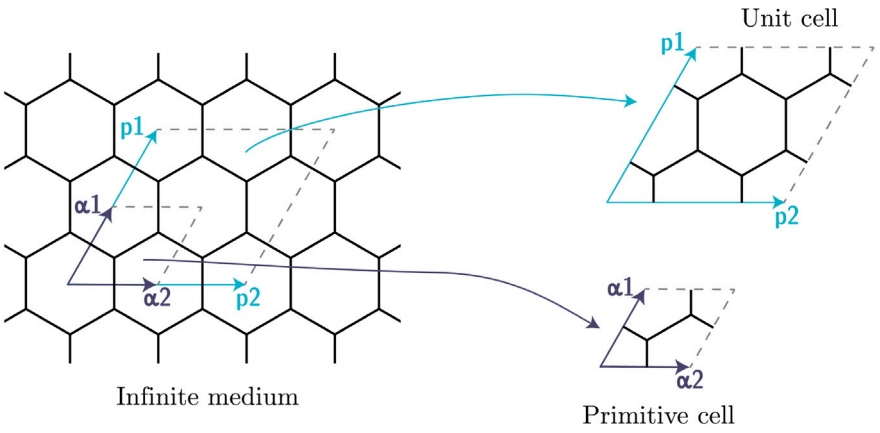

Fig. 10. Difference between primitive and unit cells when considering the bifurcation of an infinite 2D honeycomb medium.

If the influence of the initial displacement state can be neglected, the problem is simplified by setting $\underline{\mathbf{K}}_0 = 0$. The eigenvalue problem to solve is then:

$$\left[\underline{\mathbf{K}}_L + \lambda \underline{\mathbf{K}}_\sigma\right] \boldsymbol{\Phi} = \mathbf{0} \tag{25}$$

Solving Eq. (24) or Eq. (25) yields the critical load parameter λ_{cr} and its corresponding eigenvector $\boldsymbol{\Phi}$ describing the buckling "shape", more commonly called "mode". Once the buckling load and mode have been calculated, an imperfection, in the shape of the buckling mode, can be introduced in the geometry of the structure, helping the solution buckle according to the previously identified mode. This method makes it possible to study the post-bifurcated behaviour of the structure (Nguyen, 2000; De Borst et al., 2012). Specific details on the imperfection method are out of the scope of this article, but more information can be found in De Borst et al. (2012), Budiansky and Hutchinson (2003).

When dealing with more complex materials or structures which exhibit any of the previously stated mechanisms (multiple simultaneous buckling modes or an unstable post-buckling response), a more intricate non-linear analysis is required for evaluating the critical load and buckling mode of the structure.

Full-scale finite element analyses are very useful as a first approach for studying buckling in architectured materials. In most engineering applications, this type of analysis is enough to evaluate the post-buckled configurations of the structure, and their associated behaviour. Even if in most cases these methods are sufficient to assess the post-bifurcated behaviour of structures, they show certain weaknesses for more in-depth understanding of the bifurcation phenomena in architectured materials. For instance, most finite element methods are designed to miss the bifurcation point, as stopping a calculation step exactly on the bifurcation point generates an impossible equation to solve with a non-invertible tangent stiffness matrix. As a result, a more specific field studying bifurcations in architectured materials has emerged, presenting more specialised techniques from the broad field of bifurcation theory to solve such problems. These more precise studies provide an opening for the development of a design tool for architectured materials.

3.3. Bifurcation theory on infinite periodic architectured materials

Modelling the mechanical response of architectured materials is of major interest, especially for implementing their use in engineering applications. To do so, shape-reconfigurable architectured materials of infinite medium have been investigated. One of the major difficulties when studying these materials is that their buckled patterns may need a higher number of cells than the initial primitive unit cell to be described. This complicates the elaboration of homogenisation frameworks capable of modelling these materials as this phenomenon need to be taken into account. Indeed, the Representative Volume (or Surface) Element (RVE) may not be the one described by the undeformed unit cell. Another difficulty arises in determining the length-scale of the buckled pattern. The criterion for stability needs to be adapted for studying the mesoscopic scale (buckling at the cell length-scale) and macroscopic stability.

In this section we will first discuss the framework used for modelling periodic architectured materials of infinite medium. Then we will present the method and criteria for finding the bifurcation point on a loading path. Finally we will explicit how to compute the post bucking analysis of two-dimensional architectured materials.

3.3.1. Infinite periodic medium

The description of 2D shape-morphing lattice materials coincide with the one described in the work of Triantafyllidis and Schraad (1998) for rate-independent solids subjected to equi-biaxial compressive loads. It is based on the use of a unit cell and uses periodicity on its boundaries to describe the infinite medium. The major difficulty in pattern changes is, as Geymonat et al. (1993) reported in their work, that the eigenmodes of microscopic bifurcation can have a longer periodic length than the geometrical unit cell for infinite periodic solids. More specifically, if the lattice material has an initial geometric periodicity α, the initial microscopic deformation satisfies the α-periodicity up to a critical point where the periodicity may break down which creates a pattern on larger amount of cells than α. As a consequence, a unit cell of suitable size needs to be considered in order to capture the wavelength corresponding to the instability of interest. If a unit cell does not have an appropriate size, the instability might be missed by the computation.

When working with an infinite periodic medium, the choice of the periodic unit cell describing the geometry is not unique. In crystallography, where periodic infinite systems are very common, 2 types of unit cells are classically used : the primitive unit-cell which allows to reproduce the infinite structure using the smallest possible periodicity vectors, and an $n \times m$ unit-cell composed of n primitive unit cells along the first periodicity vector and m along the second (cf. Fig. 10).

As stated previously, for modelling the infinite 2D periodic structure, periodic boundary conditions are applied at boundary nodes according to the lattice periodicity vectors. Like in Elliott et al. (2006b) or (Combescure et al., 2016), we present the Lagrangian formulation for Cauchy–Born kinematics. Hence the deformed position $\mathbf{x}$ of a node i is described by:

$$\mathbf{x}_i = \underline{\mathbf{F}}(\mathbf{X}_i + \boldsymbol{\Xi}_i), \quad i \in \mathbb{N} \tag{26}$$

Where $\underline{\mathbf{F}}$ is the macroscopic deformation gradient described in the next section, $\mathbf{X}_i$ is the reference position of node i and $\boldsymbol{\Xi}_i$ is the internal periodic fluctuation, corresponding to the mesoscopic displacements in the unit-cell of node i, illustrated Fig. 11.

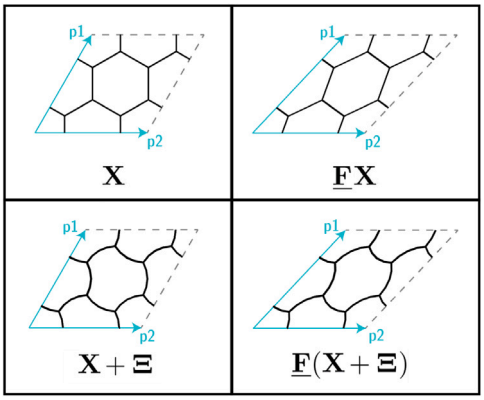

Fig. 11. Illustration of the decomposition in Eq. (26).

The displacement $\mathbf{u}$ of a node i is given by:

$$\mathbf{u}_i(\mathbf{X},t) = \mathbf{x}_i(\mathbf{X},t) - \mathbf{X}_i \tag{27}$$

Therefore:

$$\mathbf{u}_i = \left(\underline{\mathbf{F}} - \underline{\mathbf{I}}\right)\mathbf{X}_i + \underline{\mathbf{F}}\,\boldsymbol{\Xi}_i \tag{28}$$

3.3.2. Equilibrium and stability of infinite periodic architectured materials

For periodic solids, the equilibrium criterion Eq. (7) or Eq. (15) is adapted (Elliott et al., 2006b) to the description of the periodic lattice presented in the previous paragraph : Two scales need to be assessed, the macroscopic scale, represented by the deformation gradient $\mathbf{F}$ and the mesoscopic scale, represented by the internal periodic fluctuation $\boldsymbol{\Xi}$. The criterion can therefore be separated into two parts, corresponding to the scale separation. The infinite periodic medium is under stress-free equilibrium if the following conditions are satisfied simultaneously:

$$\frac{\partial \mathcal{E}(\underline{\mathbf{F}},\boldsymbol{\Xi})}{\partial \underline{\mathbf{C}}} = 0, \quad \frac{\partial \mathcal{E}(\underline{\mathbf{F}},\boldsymbol{\Xi})}{\partial \boldsymbol{\Xi}} = 0 \tag{29}$$

With $\underline{\mathbf{C}} = \underline{\mathbf{F}}^T\underline{\mathbf{F}}$ the right stretch tensor. Note that the use of the derivative with respect to the right stretch tensor is required to avoid cumbersome rigid body rotations in the equilibrium equations.

The scale separation also exists for assessing the structure's stability. For studying macroscopic stability the commonly used energy convexity condition, as described in Eq. (10), is used. This criterion only gives information on the global behaviour of the infinite structure. As a consequence, the information on if the instability is mesoscopic or macroscopic cannot be identified. Elliott et al. (2006a) determined an adjusted stability criterion to assess the structure's mesoscopic and macroscopic stability. For the body to be considered in a stable equilibrium, its energy density should be rank one convex. In other terms, its second derivative with respect to the deformation gradient should be positive:

$$\frac{\partial^2 \mathcal{E}}{\partial \underline{\mathbf{F}}^2} > 0 \tag{30}$$

Eq. (30) gives a criterion for a loss of stability of the infinite periodic architectured material with respect to macroscopic perturbations. If only periodic perturbations are of interest, the following criterion can be considered (Combescure et al., 2016):

$$\frac{\partial^2 \mathcal{E}}{\partial \boldsymbol{\Xi}^2} > 0 \tag{31}$$

This criterion will, however only predict instability for wavelengths equal to the length of the unit cell used in the computation.

3.3.3. Pattern formation in infinite periodic architectured materials

Of interest here is determining the critical wavelength of the instability that generates the pattern of interest when architectured materials are subject to compressive loads. We provide a review of the various methods which have been employed for studying this phenomenon.

Eigenvalue analysis of RVE of increasing size

Much like the method presented for finite element analysis, the mesoscopic stability of an infinite periodic honeycomb has been assessed by computing successive eigenvalue analysis of RVEs of increasing size (Bertoldi et al., 2008). With this method, the authors aimed to capture the change in periodicity of the buckled pattern by iteratively conducting the analysis. Each RVE, subject to the appropriate periodic boundary conditions, undergoes an eigenvalue analysis for its corresponding tangent stiffness matrix $\underline{\mathbf{K}}_T$. For each iteration, the critical buckling load λ_{cr} is stored and compared with the other values obtained for different RVE sizes. The wavelength of the buckling pattern is obtained by finding the RVE size corresponding to the minimum of all λ_{cr}.

Even if this method is relatively easy to implement, it presents significant drawbacks. It is impossible to compute an infinite amount of eigenvalue analyses. Even if the buckling wavelength is generally of the order of a few unit cells, some larger wavelengths which are not computed may be missed. Finally, with this method, the finite element tangent stiffness matrix computed gives information on $\frac{\partial^2 \mathcal{E}}{\partial \mathbf{u}\partial \mathbf{u}}$ and therefore does not separate macroscopic and mesoscopic scales.

Bloch Wave analysis

The Bloch wave criterion makes it possible to assess the stability of the equilibrium configuration for bounded perturbations of all wavelengths (Elliott et al., 2006a; Andersen et al., 2021; Meaud and Che, 2017; Wilcox, 1977). The criterion is equivalent to testing the previous eigenvalue analysis for all possible unit cells while only calculating on the primitive geometrical unit cell (Geymonat et al., 1993; Bertoldi et al., 2008). Bloch Wave Analysis on the primitive cell gives the loading intensity at which the instability occurs and the new periodicity of the structure.

Considering a lattice material with periodic lattice vectors $\boldsymbol{\alpha_1}$ and $\boldsymbol{\alpha_2}$ which may or may not be orthogonal. At the bifurcation point, any space function Ψ must satisfy the periodic conditions for any point $\mathbf{X}$:

$$\Psi(\mathbf{X} + l_1\boldsymbol{\alpha_1} + l_2\boldsymbol{\alpha_2}) = \Psi(\mathbf{X}), \quad (l_1,\, l_2) \in \mathbb{Z}^2, \tag{32}$$

Bloch's theorem generalises these periodic boundary conditions and states (Wilcox, 1977):

$$\Psi(\mathbf{X} + l_1\boldsymbol{\alpha_1} + l_2\boldsymbol{\alpha_2}) = \Psi(\mathbf{X})\, e^{[i\mathbf{k}\cdot\mathbf{X}]}, \tag{33}$$

With i the imaginary unit number, $\mathbf{k} = 2\pi \cdot (k_1\tilde{\boldsymbol{\alpha}}_1 + k_2\tilde{\boldsymbol{\alpha}}_2)$ the eigen-perturbation wave vector defined by the reciprocal lattice vectors $\tilde{\boldsymbol{\alpha}}_1$ and $\tilde{\boldsymbol{\alpha}}_2$ and $k_1 = \frac{1}{l_1}$, $k_2 = \frac{1}{l_2}$.

Applying Bloch's theorem to eigen-perturbations for the equilibrium configuration:

$$\delta\mathbf{u}(\mathbf{X} + l_1\boldsymbol{\alpha_1} + l_2\boldsymbol{\alpha_2}) = \delta\mathbf{u}(\mathbf{X})\, e^{[i\mathbf{k}\cdot\mathbf{X}]}, \tag{34}$$

Bloch's theorem does not determine the primitive unit cell perturbation $\delta\mathbf{u}$ as it depends on the wave vector $\mathbf{k}$. Instead, it solves an eigenvalue problem for all $\mathbf{k}$ and calculates the eigenvalues $\Lambda_i(\mathbf{k})$ associated with the eigenvectors $\delta\mathbf{u}_i$.

An equilibrium configuration is stable if the Bloch wave stability criteria is satisfied:

$$min\,(\Lambda_i(\mathbf{k})) \quad \forall i \in ndof \tag{35}$$

The critical wavelength of the bifurcated path is given by wave vector $\mathbf{k}$ and is associated with the lowest loading parameter which leads to a null eigenvalue of the tangent stiffness matrix. Reverting back to the original lattice, the wave vector $\mathbf{k}$ gives the number of cells on which the bifurcation takes place.

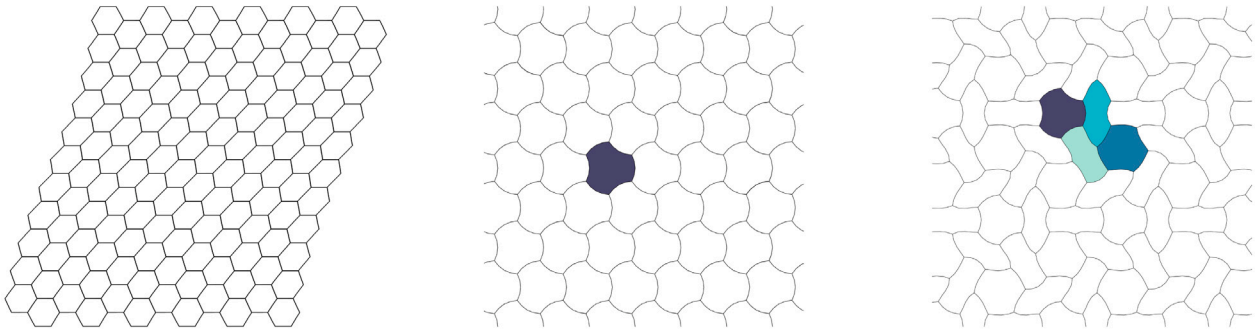

Fig. 12. Illustration of stability criteria : (a) Rank one convexity instability, (b) Primitive cell instability, (c) Bloch wave instability.

The Bloch wave analysis can be implemented in standard finite element software by separating the real and imaginary parts of the displacements into two separate tensors. However, it takes a lot of computational resources since the eigenvalue analysis must be carried out for all values of wave vector $\mathbf{k}$ in its range of variation. However, these computations are completely independent between one another and could be easily parallelised. Furthermore, all these computations take place on the smallest possible periodic unit cell (the primitive unit cell) therefore limiting the computation cost even more. Finally, using crystallography, the problem can be reduced to the first irreducible Brillouin Zone (Combescure et al., 2016) thus limiting the range of variation for the wave vector $\mathbf{k}$.

Examples of bifurcated modes captured by the three criteria presented so far are proposed Fig. 12.

3.4. Group-theoretic bifurcation theory

In most cases, a bifurcation phenomena generates a loss of symmetry in the bifurcated path. Such bifurcation is referred to as a "symmetry-breaking bifurcation", as the symmetry of the bifurcated path is often (Golubitsky et al., 1988; Ohno et al., 2002; Hoyle, 2006; Ikeda and Murota, 2010) less than the symmetry of the original structure. When considering periodic architectured materials, both rotational-type symmetries, i.e. point-group symmetries, and translational symmetries can be broken. The latter is noticed by a change in the RVE shape and size before and after bifurcation. The mechanisms of such pattern changes are subject to rules which can be explained by group theoretic methods (Golubitsky et al., 1988; Hoyle, 2006; Ikeda and Murota, 2010).

As of today, two procedures exist for finding the post bifurcation behaviour of honeycombs. The first method is a rather theoretical approach based on the Equivariant Branching Lemma (EBL) as first described by Vanderbauwhede (1980). To our knowledge, this method has only been used for simple point-groups and never applied in this field of materials science. The second method, used for studying the flower-like mode in Saiki et al. (2005) is based on a Lyapunov–Schmidt–Koiter (LSK) decomposition of the system's governing equations. After assessing the symmetry of the problem from a mathematical standpoint, authors use LSK decomposition to determine the post-bifurcated branches and the symmetry of the associated bifurcated solution (Saiki et al., 2005; Ikeda and Murota, 2010; Combescure et al., 2016, 2020).

The aim of this section is to present the second method in detail. It is used in Saiki et al. (2005) to determine the nature of the flower patterns which appear in honeycombs under equi-biaxial compression. The structure's behaviour is governed by a system of non-linear equilibrium equations, as in Eq. (15), which can be rewritten, in the framework of bifurcation theory (Hoyle, 2006), as:

$$\mathcal{E}_{,\mathbf{u}}(\mathbf{u},\lambda) = \mathbf{F}(\mathbf{u},\lambda) = 0, \quad \mathbf{F} : \mathbb{R}^N \times \mathbb{R} \longrightarrow \mathbb{R}^N \tag{36}$$

Where $\mathbf{u}$ is the displacement vector of the system and λ the loading parameter and the notation $\mathcal{E}_{,\mathbf{u}}$ stands for the Fréchet derivative of the system's total potential energy.

The principal path is the set of solution points $(\mathbf{u}_0, \lambda_0)$ satisfying the equilibrium Eq. (36) and passing through the point $(0,0)$. Along the principal path, there can be *critical points* $(\mathbf{u}_c, \lambda_c)$ at which the system's Jacobian matrix becomes singular. At these critical points, we can find a set of basis vectors of $\{\boldsymbol{\eta}_{ic},\ i = 1,\dots,N\} \in \mathbb{R}^N$, spanning what is called the kernel, or the null space $\mathcal{N}$ of $\underline{\mathbf{J}}(\mathbf{u}_c, \lambda_c)$, satisfying:

$$\underline{\mathbf{J}}(\mathbf{u}_c,\lambda_c)\boldsymbol{\eta}_{ic} = \mathcal{E}_{,\mathbf{uu}}(\mathbf{u}_c,\lambda_c)\boldsymbol{\eta}_{ic} = \mathbf{0}, \quad \forall i = 1,\dots,m. \tag{37}$$

Where $m \in \mathbb{N}$ is the dimension of the kernel of $\underline{\mathbf{J}}(\mathbf{u}_c, \lambda_c)$. Note that, in the case of equilibrium of mechanical systems, the Jacobian matrix is the tangent stiffness matrix.

The multiplicity of the critical point is equal to m, the number of null eigenvalues of $\underline{\mathbf{J}}(\mathbf{u}_c, \lambda_c)$ at the critical point. If the multiplicity is equal to 1, not much needs to be done since the dimension of the kernel is uni-dimensional and thus only one equilibrium branch stems from the critical point. However, as soon as the multiplicity of the critical point becomes larger, the question of finding the equilibrium paths that are lines in a multidimensional kernel arises. In order to find the tangents to these lines, Lyapunov–Schmidt–Koiter decomposition is employed as follows.

The Lyapunov–Schmidt–Koiter decomposition method (Triantafyllidis and Peek, 1992) is used to investigate the equilibrium around the critical point $(\mathbf{u}_c, \lambda_c)$. According to this method, the increment of the displacement $\delta\mathbf{u} = \mathbf{u} - \mathbf{u}_c$ due to an increment in the load $\Delta\lambda \equiv \lambda - \lambda_c$ is decomposed in two components: (i) one component $\sum_i^m \xi_i \boldsymbol{\eta}_{ic}$, where ξ_i is the projection of $\delta\mathbf{u}$ on $\boldsymbol{\eta}_{ic}$, is on the kernel $\mathcal{N}$ of $J(\mathbf{u}_c, \lambda_c)$ and (ii) the other component $\delta\mathbf{v}$ is in $\mathcal{N}^\perp$, i.e. orthogonal to the first, namely:

$$\mathbf{u} = \mathbf{u}_c + \sum_i^m \xi_i \boldsymbol{\eta}_{ic} + \delta\mathbf{v} \qquad \delta\mathbf{v} \in \mathcal{N}^\perp, \quad \xi_i \in \mathbb{R} \tag{38}$$

Therefore, the unknown displacement increment $\delta\mathbf{u}$ is in essence replaced by the equivalent set of unknowns $(\delta\mathbf{v}, \xi_i), i = 1,\dots,m$. Consequently, the equilibrium Eq. (36) can be replaced by two sets of equations in $\mathcal{N}$ and $\mathcal{N}^\perp$:

$$\mathcal{E}_{,\delta\mathbf{v}}(\mathbf{u}_c + \sum_{i=1}^m \xi_i \boldsymbol{\eta}_{ic} + \delta\mathbf{v}, \lambda_c + \Delta\lambda)\delta\mathbf{v} = 0, \quad \forall \delta\mathbf{v} \in \mathcal{N}^\perp \tag{39}$$

and

$$\mathcal{E}_{,\xi_i}(\mathbf{u}_c + \sum_{i=1}^m \xi_i \boldsymbol{\eta}_{ic} + \delta\mathbf{v}, \lambda_c + \Delta\lambda)\boldsymbol{\eta}_{ic} = 0, \quad \forall i = 1,\dots,m \tag{40}$$

By definition, the projected equilibrium equations in the space orthogonal to the kernel have a positive definite Jacobian matrix $\mathcal{E}_{,\delta\mathbf{v}\delta\mathbf{v}}$, thus the solution of Eq. (39) is smooth and unique in the neighbourhood of the critical point, hence easy to determine. By focusing on the equilibrium Eq. (40) in the kernel of the Jacobian matrix at the critical

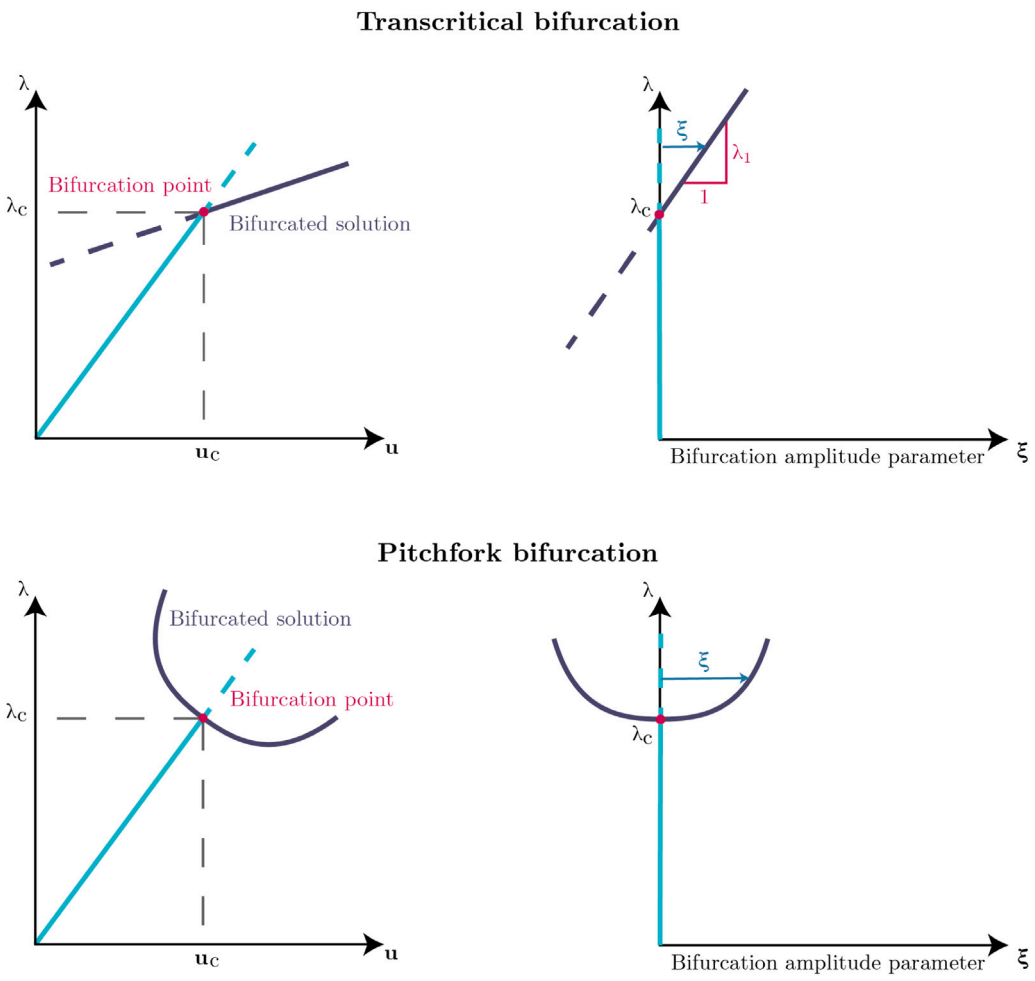

Fig. 13. *Schematic representations of LSK decomposition about the bifurcation point in the case of transcritical and pitchfork bifurcations. Left : representations of equilibrium paths in terms of loading parameter and displacement amplitude; Right: representations of equilibrium paths in terms of loading parameter and bifurcation amplitude parameter.*

point these equations can be expanded using a Taylor series expansion about the critical point $(\mathbf{u}_c, \lambda_c)$, or equivalently about $(\xi_i, \Delta\lambda) = (0,0)$ if the expansion stays in the kernel:

$$0 = \Delta\lambda \mathcal{E}_{,\mathbf{u}\lambda}\,\mathbf{u}_i + \frac{1}{2}\left[\sum_{j=1}^{m}\sum_{k=1}^{m}\xi_j\xi_k\mathcal{E}_{ijk} + 2\Delta\lambda\sum_{j=1}^{m}\xi_j\mathcal{E}_{ij\lambda}\right] + \frac{1}{6}\left[\sum_{j=1}^{m}\sum_{k=1}^{m}\sum_{l=1}^{m}\xi_j\xi_k\xi_l\mathcal{E}_{ijkl} + \cdots\right] + \cdots \tag{41}$$

where $\mathcal{E}_{ijk} \equiv \mathcal{E}_{,\mathbf{uuu}}\,\mathbf{u}_i\mathbf{u}_j\mathbf{u}_k$, $\mathcal{E}_{ij\lambda} \equiv \mathcal{E}_{,\mathbf{uu}\lambda}\,\mathbf{u}_i\mathbf{u}_j + \mathcal{E}_{,\mathbf{uuu}}\left(\frac{d\mathbf{u}_0}{d\lambda}\right)\mathbf{u}_i\mathbf{u}_j$ etc.

The above equation should provide a relation between the ξ_i and $\Delta\lambda$ along the equilibrium paths passing through the critical point. In order to determine this relation, we introduce a *bifurcation amplitude parameter* ξ, defined as the projection of $\delta\mathbf{u}$ on the unit tangent of the equilibrium path $\mathbf{t} = \sum_{i=1}^{m}\alpha_i\boldsymbol{\eta}_{ic}$. Note that ξ acts like an arclength parameter along the bifurcating path. The question is then to find the tangent parameters α_i defining the tangent to the equilibrium paths at the critical point.

Assume that $\Delta\lambda$ and ξ_i can be put in Taylor series expansions in terms of ξ:

$$\xi_i(\xi) = \alpha_i^1\xi + \alpha_i^2\frac{\xi^2}{2} + \cdots \tag{42}$$

$$\Delta\lambda(\xi) = \lambda_1\xi + \lambda_2\frac{\xi^2}{2} + \cdots \tag{43}$$

Where $\xi = \mathbf{u} - \overset{0}{\mathbf{u}}, \sum_{i=1}^{m}\alpha_i^1\boldsymbol{\eta}_{ic}$.

These expansions can be inserted into the projected equilibrium Eq. (41).

From this point, two cases are distinguished:

1. $\mathcal{E}_{,\mathbf{u}\lambda}\,\mathbf{u}_i \neq 0$ in which case the λ_i coefficients in Eq. (43) can be determined uniquely with $\lambda_1 = 0$. It is the case of a *limit load* where there is only one equilibrium branch through the critical point and the solution is unique. The unique equilibrium branch reaches a load extremum at the critical point since the sign of $\Delta\lambda$ is independent to the sign of ξ. This case is easy to compute and will be disregarded for the rest of this paragraph.
2. $\mathcal{E}_{,\mathbf{u}\lambda}\,\mathbf{u}_i = 0$ where the $\Delta\lambda - \xi_i$ relation is no longer unique and the critical point is a multiple bifurcation point of multiplicity m. The $\Delta\lambda - \xi_i$ relation is then described by the equation:

$$\frac{1}{2}\left[\sum_{j=1}^{m}\sum_{k=1}^{m}\alpha_j^1\alpha_k^1\mathcal{E}_{ijk} + 2\lambda_1\sum_{j=1}^{m}\alpha_j^1\mathcal{E}_{ij\lambda}\right] + \frac{\xi}{6}\left[\sum_{j=1}^{m}\sum_{k=1}^{m}\sum_{l=1}^{m}\alpha_j^1\alpha_k^1\alpha_l^1\mathcal{E}_{ijkl} + 3\lambda_2\sum_{j=1}^{m}\alpha_j^1\mathcal{E}_{ij\lambda}\right] + \cdots = 0 \tag{44}$$

This latter case of multiple bifurcation point can be further subdivised into two subcases whether $\mathcal{E}_{ijk} \neq 0$, thus leading to a transcritical bifurcation or $\mathcal{E}_{ijk} = 0$ leading to a pitchfork bifurcation. As Eq. (44) is true for all ξ, the two subcases above lead to either $\lambda_1 \neq 0$ which yields a transcritical bifurcation, or $\lambda_1 = 0$ which yields a pitchfork bifurcation (see Fig. 13).

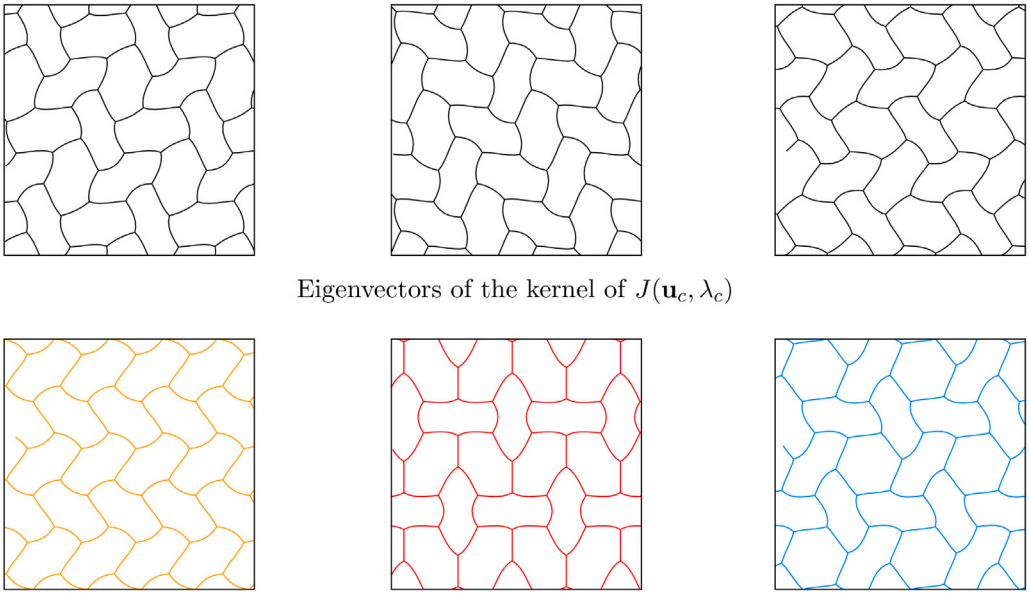

Fig. 14. Illustration of the eigenvectors of the kernel of $\underline{\mathbf{J}}(\mathbf{u}_c, \lambda_c)$ when the specimen is subject to equibiaxial compression. The top three images are the eigenvectors obtained using the previously presented method. The bottom three images are the projections of the eigenvectors onto the symmetry-adapted basis adapted from (Combescure et al., 2016).

In any case, in order to pursue the computation of the bifurcated branch, one has to be able to predict the non-null leading order parameters α_i^1 and λ_1 or λ_2. This is done by solving the non-linear coupled Eq. (44) for the unknowns (α_i^1, λ_1 or λ_2). In the traditional case of simple bifurcations, where only one bifurcated branch stems from the bifurcation point, there is only one $\xi_i, \quad i = 1$ and thus only one $\alpha_i^1, \quad i = 1$ and the computation is straightforward. However, when multiple bifurcation points arises, a large number of combinations of α_i can be found and not all of them corresponds to an equilibrium path, meaning that not all of them are solutions to Eq. (44). Unfortunately, the expressions for the higher order tensors $\mathcal{E}_{ijk}, \mathcal{E}_{ij\lambda}$ and $\mathcal{E}_{ijkl}$ are complex and often not available in standard finite element codes. This is where symmetry group theory comes into play to predict the general shape of these tensors thanks to representation theory (Auffray et al., 2017).

If the system described by $\mathbf{F}(\mathbf{u}, \lambda)$ is symmetric, it satisfies the equivariance condition of its symmetric group G for all independent vector $\mathbf{u}$:

$$\underline{\mathbf{T}}(g)\mathbf{F}(\mathbf{u}, \lambda) = \mathbf{F}(\underline{\mathbf{T}}(g)\mathbf{u}, \lambda), \quad \forall g \in G \tag{45}$$

Where g is an element of the group G, $\underline{\mathbf{T}}$ is a $N \times N$ matrix representation of G on the N-dimensional space of $\mathbf{u}$.

If $(\mathbf{u}_c, \lambda_c)$ is a critical point on the principal path, then the solution $\mathbf{u}_c$ in invariant under the action of any group element $g \in G$:

$$\underline{\mathbf{T}}(g)\mathbf{u}_c = \mathbf{u}_c, \quad \forall g \in G \tag{46}$$

In the case of a *symmetry-breaking* bifurcation, the symmetry of the solutions $\overset{1}{\mathbf{u}}$ on the bifurcated branch, after bifurcation, is lower than the symmetry of the critical point $(\mathbf{u}_c, \lambda_c)$. It is defined by the subgroup H satisfying:

$$H = \{g \in G \,/\, \underline{\mathbf{T}}(g)\overset{1}{\mathbf{u}} = \overset{1}{\mathbf{u}}\}, \quad H \subseteq G \tag{47}$$

Both $\overset{1}{\mathbf{u}}$ and $\underline{\mathbf{T}}(g)\overset{1}{\mathbf{u}}$ are solutions of Eq. (36), for all $g \in H$.

All the representations of a symmetry group can be broken down to irreducible representations, also called irreps (McWeeny, 2002). In the case of finite symmetry groups, these irreps are tabulated and they can be related to symmetry breaking (Golubitsky et al., 1988, 1984; Hoyle, 2006; Ikeda and Murota, 2010). Let $\underline{\mathbf{T}}^\mu$ be an irreducible representation of G and n^μ the dimension of this irreducible representation. The kernel of $\underline{\mathbf{T}}^\mu$ is the subgroup defined by:

$$G^\mu = \{g \in G \,/\, \underline{\mathbf{T}}^\mu(g) = \underline{\mathbf{I}}_{n^\mu}\} \tag{48}$$

With I_{n^μ} the identity matrix of dimension n^μ.

At the critical point $(\mathbf{u}_c, \lambda_c)$, the symmetry of the kernel of $\underline{\mathbf{J}}(\mathbf{u}_c, \lambda_c)$ and G^μ coincide. Therefore, G^μ also satisfies:

$$G^\mu = \{g \in G \,/\, \underline{\mathbf{T}}(g)\overset{1}{\mathbf{u}} = \overset{1}{\mathbf{u}}, \ \forall \overset{1}{\mathbf{u}} \in ker(\underline{\mathbf{J}}(\mathbf{u}_c, \lambda_c))\} \tag{49}$$

As a consequence, by studying the eigenvectors belonging to the kernel of $\underline{\mathbf{J}}(\mathbf{u}_c, \lambda_c)$, it is possible to determine the subgroup G^μ of the solutions $\overset{1}{\mathbf{u}}$ along the bifurcating equilibrium paths. Along these paths, we now have equivariance of equilibrium equations, like in Eq. (46), but related to subgroup G^μ instead of full group G. As a result, all the Taylor series expansions carried out following Lyapunov–Schmidt–Koiter extension, into the null space of $\underline{\mathbf{J}}(\mathbf{u}_c, \lambda_c)$ also satisfy the equivariance condition with respect to subgroup G^μ. This applies particularly to Eq. (44). Using representation theory, one can then build the symmetry adapted generic shapes of higher order tensors $\mathcal{E}_{ijk}, \mathcal{E}_{ij\lambda}$ and $\mathcal{E}_{ijkl}$, related to subgroup G^μ and, in special cases, have enough information to solve Eq. (44). Indeed, $\mathcal{E}_{ijk}, \mathcal{E}_{ij\lambda}$ and $\mathcal{E}_{ijkl}$ can be projected onto the *symmetry adapted basis* of the problem (Golubitsky et al., 1988; McWeeny, 2002) to obtain the bifurcated solutions (see Fig. 14).

This was the case of double and triple bifurcations appearing when studying the instabilities of hexagonal honeycombs studied in Saiki et al. (2005), Ikeda and Murota (2010), Combescure et al. (2016, 2020). However, in more complex cases, the generic shapes of higher order tensors might not be enough to solve equilibrium equations projected in the null space and different approaches should be taken to find the bifurcated equilibrium path stemming from a multiple bifurcation point. Among these different approaches one can think first of the group theoretical approach based on the Equivariant Branching Lemma (EBL) described by Vanderbauwhede (1980), but also of more numerical methods like the perturbation or imperfection based methods briefly discussed in 3.2.2.

4. Conclusion

Understanding the mechanical behaviour and properties of architectured materials is necessary to encourage their use in real-life applications. The honeycomb lattice experiments, presented in this article, were the starting point for elaborating theoretical and computational methods and have enriched our understanding of the underlying mechanisms of pattern generation in architectured materials caused by instabilities. As of today, thanks to these newly developed methods, classical problems (Combescure et al., 2020; Pandurangi et al., 2022) are still revisited for a more accurate description and a better understanding of the phenomenon whilst taking into account possible computational obstacles.

Studies on pattern generation are for the most part conducted on 2D architectured materials to reduce the computational complexity of the problem. Even with such materials, significant drawbacks can be found. For instance, in addition to being computationally costly classical finite element analysis cannot account for the multiplicity of the bifurcated modes of deformation available for a given geometry, and its computational cost increases drastically with specifically designed algorithms for stability analysis (Al Kotob et al., 2020). Nevertheless, all the previous discussions and findings can be extended to 3D using the same theories presented in this review (Babaee et al., 2013; Shim et al., 2012; Frenzel et al., 2017), but will come at a higher computational cost. It is therefore essential to continue to develop and adapt existing models to be even more accurate and efficient.

A first step in creating such techniques could be to combine the recent improvements in modelling pattern generating architectured materials. Indeed, the insight provided by group theory on symmetry-breaking bifurcations has provided a powerful tool which could lead to more complete description of the phenomenon, giving more information on how to predict the post-bifurcated patterns based on the symmetry of the structure. Combined with a Bloch wave analysis for determining the size of the RVE, this could become a first step to tackle the problem from a design point of view – predicting the experiments – rather than carrying out post-observation analyses and could significantly increase the performance of current models.

Observations and breakthroughs in other fields of research which exhibit pattern-generating arrangements have significantly improved modelling methodologies for studying instability-induced pattern generation in architectured materials. For instance, the use of Bloch's theorem previously used by crystallographers has boosted the efficiency and reliability of the prediction of the size of the RVE. Fluid mechanics has also provided much of the background on bifurcation theory and group theory presented in this review (Hoyle, 2006). The stability criterion for the infinite periodic medium is transferred from the stability criterion of martensitic transformations formulated by Elliott et al. (2006a). Chemistry could be a source of inspiration as studying a molecule's symmetry group determines its physical properties (Bunker and Jensen, 2018). Therefore, we highlight the importance of identifying and studying relevant experiments as it is what could continue to inspire new modelling approaches in the future.

Analogously, similar phenomena observed in other areas could benefit from the techniques presented in this review. For instance, Miyoshi et al. (2021) have found matching patterns to those of mode I, II and III of the regular hexagonal honeycomb (amongst others) caused by dimples in a gel film bonded to a soft substrate when in contact with a solvent. The tools used to predict the patterns on the substrate are identical to the ones presented in this article for architectured materials : finite element eigenvalue analyses to compute the bifurcation point and the introduction of an imperfection to determine the post-buckling patterns. We can imagine that this particular application could benefit from the group-theoretical methods for symmetry-breaking bifurcations developed in the case of hexagonal honeycombs for a more complete understanding of the phenomenon. These techniques could also be used for a more complete understanding of pattern-generating structures such as the periodic buckling structures in free-standing graphene bilayers (Mao et al., 2011), the yoshimura pattern on twisted cylinders (Hunt and Ario, 2005), pattern changes in switchable metal–organic frameworks (Krause et al., 2019; Evans et al., 2016) and even cortical folding (Jalil Razavi et al., 2015).

Declaration of competing interest

The authors declare that they have no known competing financial interests or personal relationships that could have appeared to influence the work reported in this paper.

Data availability

No data was used for the research described in the article

Acknowledgements

This work was supported by Agence Nationale de la Recherche, France through the ANR MAX-OASIS project (Grant No. ANR-19-CE08-0005).

References

Al Kotob, M., Combescure, C., Mazière, M., Rose, T., Forest, S., 2020. A general and efficient multistart algorithm for the detection of loss of ellipticity in elastoplastic structures. Internat. J. Numer. Methods Engrg. 121 (5), 842–866.

Andersen, M.N., Wang, F., Sigmund, O., 2021. On the competition for ultimately stiff and strong architected materials. Mater. Des. 198, 109356. http://dx.doi.org/10.1016/j.matdes.2020.109356, URL: https://www.sciencedirect.com/science/article/pii/S0264127520308923.

Ashby, M., Bréchet, Y., 2003. Designing hybrid materials. Acta Mater. 51, 5801–5821. http://dx.doi.org/10.1016/S1359-6454(03)00441-5.

Auffray, N., Kolev, B., Olive, M., 2017. Handbook of bi-dimensional tensors: Part I: Harmonic decomposition and symmetry classes. Math. Mech. Solids 22 (9), 1847–1865.

Babaee, S., Overvelde, J.T.B., Chen, E.R., Tournat, V., Bertoldi, K., 2016. Reconfigurable origami-inspired acoustic waveguides. Sci. Adv. 2 (11), e1601019. http://dx.doi.org/10.1126/sciadv.1601019, URL: https://advances.sciencemag.org/content/2/11/e1601019.

Babaee, S., Shim, J., Weaver, J.C., Chen, E.R., Patel, N., Bertoldi, K., 2013. 3D soft metamaterials with negative Poisson's ratio. Adv. Mater. 25 (36), 5044–5049. http://dx.doi.org/10.1002/adma.201301986, URL: https://onlinelibrary.wiley.com/doi/abs/10.1002/adma.201301986.

Barthelat, F., 2015. Architectured materials in engineering and biology: fabrication, structure, mechanics and performance. Int. Mater. Rev. 60 (8), 413–430. http://dx.doi.org/10.1179/1743280415Y.0000000008.

Bertoldi, K., 2017. Harnessing instabilities to design tunable architected cellular materials. Annu. Rev. Mater. Res. 47 (1), 51–61. http://dx.doi.org/10.1146/annurev-matsci-070616-123908.

Bertoldi, K., Boyce, M.C., 2008. Mechanically triggered transformations of phononic band gaps in periodic elastomeric structures. Phys. Rev. B 77 (5), 052105. http://dx.doi.org/10.1103/PhysRevB.77.052105, URL: https://link.aps.org/doi/10.1103/PhysRevB.77.052105.

Bertoldi, K., Boyce, M.C., Deschanel, S., Prange, S.M., Mullin, T., 2008. Mechanics of deformation-triggered pattern transformations and superelastic behavior in periodic elastomeric structures. J. Mech. Phys. Solids 56 (8), 2642–2668. http://dx.doi.org/10.1016/j.jmps.2008.03.006, URL: http://www.sciencedirect.com/science/article/pii/S0022509608000434.

Bertoldi, K., Vitelli, V., Christensen, J., van Hecke, M., 2017. Flexible mechanical metamaterials. Nat. Rev. Mater. 2 (11), 1–11. http://dx.doi.org/10.1038/natrevmats.2017.66, URL: https://www.nature.com/articles/natrevmats201766.

Bigoni, D., 2012. Nonlinear Solid Mechanics: Bifurcation Theory and Material Instability. Cambridge University Press.

Blees, M.K., Barnard, A.W., Rose, P.A., Roberts, S.P., McGill, K.L., Huang, P.Y., Ruyack, A.R., Kevek, J.W., Kobrin, B., Muller, D.A., McEuen, P.L., 2015. Graphene kirigami. Nature 524 (7564), 204–207. http://dx.doi.org/10.1038/nature14588, URL: https://www.nature.com/articles/nature14588.

Bouaziz, O., Bréchet, Y., Embury, J.D., 2008. Heterogeneous and architectured materials: a possible strategy for design of structural materials. Adv. Eng. Mater. 10 (1–2), 24–36.

Brechet, Y., Embury, J.D., 2013. Architectured materials: Expanding materials space. Architectured Materials, Scr. Mater. Architectured Materials, 68 (1), 1–3. http://dx.doi.org/10.1016/j.scriptamat.2012.07.038.URL: https://www.sciencedirect.com/science/article/pii/S135964621200499X,

Budiansky, B., Hutchinson, J.W., 2003. A survey of some buckling problems. J. Spacecr. Rockets 40 (6), 918–923.

Bufler, H., 1993. Conservative systems, potential operators and tangent stiffness: reconsideration and generalization. Arch. Appl. Mech. 63 (1), 51–58.

Bunker, P.R., Jensen, P., 2018. Fundamentals of Molecular Symmetry. CRC Press.

Chen, Y., Scarpa, F., Remillat, C., Farrow, I., Liu, Y., Leng, J., 2014. Curved Kirigami SILICOMB cellular structures with zero Poisson's ratio for large deformations and morphing. J. Intell. Mater. Syst. Struct. 25 (6), 731–743. http://dx.doi.org/10.1177/1045389X13502852.

Christensen, J., Kadic, M., Kraft, O., Wegener, M., 2015. Vibrant times for mechanical metamaterials. Mrs Commun. 5 (3), 453–462.

Chung, J., Waas, A.M., 2002. Compressive response of circular cell polycarbonate honeycombs under inplane biaxial static and dynamic loading. Part I: experiments. Int. J. Impact Eng. 27 (7), 729–754. http://dx.doi.org/10.1016/S0734-743X(02)00011-8, URL: https://www.sciencedirect.com/science/article/pii/S0734743X02000118.

Combescure, C., Elliott, R.S., Triantafyllidis, N., 2020. Deformation patterns and their stability in finitely strained circular cell honeycombs. J. Mech. Phys. Solids 142, 103976. http://dx.doi.org/10.1016/j.jmps.2020.103976, URL: http://www.sciencedirect.com/science/article/pii/S0022509620302118.

Combescure, C., Henry, P., Elliott, R.S., 2016. Post-bifurcation and stability of a finitely strained hexagonal honeycomb subjected to equi-biaxial in-plane loading. Int. J. Solids Struct. 88–89, 296–318. http://dx.doi.org/10.1016/j.ijsolstr.2016.02.016, URL: http://www.sciencedirect.com/science/article/pii/S0020768316000780.

Curatolo, M., 2018. Effective negative swelling of hydrogel-solid composites. Extreme Mech. Lett. 25, 46–52. http://dx.doi.org/10.1016/j.eml.2018.10.010, URL: https://www.sciencedirect.com/science/article/pii/S2352431618302050.

Danas, K., Kankanala, S., Triantafyllidis, N., 2012. Experiments and modeling of iron-particle-filled magnetorheological elastomers. J. Mech. Phys. Solids 60 (1), 120–138.

De Borst, R., Crisfield, M.A., Remmers, J.J., Verhoosel, C.V., 2012. Nonlinear finite element analysis of solids and structures. John Wiley & Sons.

Dunlop, J.W., Weinkamer, R., Fratzl, P., 2011. Artful interfaces within biological materials. Mater. Today 14 (3), 70–78.

Elliott, R.S., Shaw, J.A., Triantafyllidis, N., 2006a. Stability of crystalline solids—II: Application to temperature-induced martensitic phase transformations in a bi-atomic crystal. J. Mech. Phys. Solids 54 (1), 193–232. http://dx.doi.org/10.1016/j.jmps.2005.07.008, URL: http://www.sciencedirect.com/science/article/pii/S002250960500147X.

Elliott, R.S., Triantafyllidis, N., Shaw, J.A., 2006b. Stability of crystalline solids—I: Continuum and atomic lattice considerations. J. Mech. Phys. Solids 54 (1), 161–192. http://dx.doi.org/10.1016/j.jmps.2005.07.009, URL: http://www.sciencedirect.com/science/article/pii/S0022509605001468.

Ellobody, E., 2014. Chapter 5 - Finite element analysis of steel and steel-concrete composite bridges. In: Ellobody, E. (Ed.), Finite Element Analysis and Design of Steel and Steel-Concrete Composite Bridges. Butterworth-Heinemann, Oxford, pp. 469–554. http://dx.doi.org/10.1016/B978-0-12-417247-0.00005-3, URL: https://www.sciencedirect.com/science/article/pii/B9780124172470000053.

Estrin, Y., Bréchet, Y., Dunlop, J., Fratzl, P., 2019. Architectured Materials in Nature and Engineering: Archimats. Springer.

Evans, J.D., Bocquet, L., Coudert, F.-X., 2016. Origins of negative gas adsorption. Chem 1 (6), 873–886.

Fang, H., Chu, S.-C.A., Xia, Y., Wang, K.-W., 2018. Programmable self-locking origami mechanical metamaterials. Adv. Mater. 30 (15), 1706311. http://dx.doi.org/10.1002/adma.201706311, URL: https://onlinelibrary.wiley.com/doi/abs/10.1002/adma.201706311.

Feenstra, D., Banerjee, R., Fraser, H., Huang, A., Molotnikov, A., Birbilis, N., 2021. Critical review of the state of the art in multi-material fabrication via directed energy deposition. Curr. Opin. Solid State Mater. Sci. 25 (4), 100924.

Frenzel, T., Kadic, M., Wegener, M., 2017. Three-dimensional mechanical metamaterials with a twist. Science 358 (6366), 1072–1074.

Gao, C., Slesarenko, V., Boyce, M.C., Rudykh, S., Li, Y., 2018. Instability-induced pattern transformation in soft metamaterial with hexagonal networks for tunable wave propagation. Sci. Rep. 8 (1), 11834. http://dx.doi.org/10.1038/s41598-018-30381-1, URL: https://www.nature.com/articles/s41598-018-30381-1.

Geymonat, G., Müller, S., Triantafyllidis, N., 1993. Homogenization of nonlinearly elastic materials, microscopic bifurcation and macroscopic loss of rank-one convexity. Arch. Ration. Mech. Anal. 122 (3), 231–290. http://dx.doi.org/10.1007/BF00380256.

Gibson, I.J., Ashby, M.F., 1982. The mechanics of three-dimensional cellular materials. Proc. R. Soc. Lond. Ser. A Math. Phys. Eng. Sci. 382 (1782), 43–59. http://dx.doi.org/10.1098/rspa.1982.0088, URL: https://royalsocietypublishing.org/doi/abs/10.1098/rspa.1982.0088.

Gibson, L., Ashby, M., 1988. Cellular Solids, 1988. Pergamon, Oxford.

Golubitsky, M., Stewart, I., schaeffer, d., 1988. Singularities and Groups in Bifurcation Theory: Volume II. In: Applied Mathematical Sciences, Singularities and Groups in Bifurcation Theory, Springer-Verlag, New York, http://dx.doi.org/10.1007/978-1-4612-4574-2, URL: https://www.springer.com/gp/book/9780387966526.

Golubitsky, M., Swift, J.W., Knobloch, E., 1984. Symmetries and pattern selection in Rayleigh-Bénard convection. Physica D 10 (3), 249–276. http://dx.doi.org/10.1016/0167-2789(84)90179-9, URL: https://www.sciencedirect.com/science/article/pii/0167278984901799.

Guiducci, L., Fratzl, P., Bréchet, Y.J., Dunlop, J.W., 2014. Pressurized honeycombs as soft-actuators: a theoretical study. J. R. Soc. Interface 11 (98), 20140458.

Guiducci, L., Razghandi, K., Bertinetti, L., Turcaud, S., Rüggeberg, M., Weaver, J.C., Fratzl, P., Burgert, I., Dunlop, J.W., 2016. Honeycomb actuators inspired by the unfolding of ice plant seed capsules. PLoS One 11 (11), e0163506.

Guiducci, L., Weaver, J.C., Bréchet, Y.J., Fratzl, P., Dunlop, J.W.C., 2015. The geometric design and fabrication of actuating cellular structures. Adv. Mater. Interfaces 2 (11), 1500011.

Guo, X.E., Gibson, L.J., 1999. Behavior of intact and damaged honeycombs: a finite element study. Int. J. Mech. Sci. 41 (1), 85–105. http://dx.doi.org/10.1016/S0020-7403(98)00037-X, URL: https://www.sciencedirect.com/science/article/pii/S002074039800037X.

Harrington, M.J., Razghandi, K., Ditsch, F., Guiducci, L., Rueggeberg, M., Dunlop, J.W., Fratzl, P., Neinhuis, C., Burgert, I., 2011. Origami-like unfolding of hydro-actuated ice plant seed capsules. Nature Commun. 2 (1), 1–7.

He, Y., Zhou, Y., Liu, Z., Liew, K.M., 2017. Pattern transformation of single-material and composite periodic cellular structures. Mater. Des. 132, 375–384. http://dx.doi.org/10.1016/j.matdes.2017.07.022, URL: https://www.sciencedirect.com/science/article/pii/S0264127517306834.

He, Y., Zhou, Y., Liu, Z., Liew, K.M., 2018. Buckling and pattern transformation of modified periodic lattice structures. Extreme Mech. Lett. 22, 112–121. http://dx.doi.org/10.1016/j.eml.2018.05.011, URL: https://www.sciencedirect.com/science/article/pii/S2352431618300841.

Hoyle, R., 2006. Pattern Formation: an Introduction To Methods. Cambridge University Press.

Hu, J., He, Y., Lei, J., Liu, Z., 2013. Novel mechanical behavior of periodic structure with the pattern transformation. Theor. Appl. Mech. Lett. 3 (5), 054007. http://dx.doi.org/10.1063/2.1305407, URL: https://www.sciencedirect.com/science/article/pii/S2095034915302634.

Hunt, G.W., Ario, I., 2005. Twist buckling and the foldable cylinder: an exercise in origami. Int. J. Non-Linear Mech. 40 (6), 833–843.

Ikeda, K., Murota, K., 2010. Imperfect Bifurcation in Structures and Materials: Engineering Use of Group-Theoretic Bifurcation Theory. Springer Science & Business Media.

Jalil Razavi, M., Zhang, T., Liu, T., Wang, X., 2015. Cortical folding pattern and its consistency induced by biological growth. Sci. Rep. 5 (1), 14477.

Kadic, M., Milton, G.W., van Hecke, M., Wegener, M., 2019. 3D metamaterials. Nat. Rev. Phys. 1 (3), 198–210.

Kang, S.H., Shan, S., Noorduin, W.L., Khan, M., Aizenberg, J., Bertoldi, K., 2013. Buckling-induced reversible symmetry breaking and amplification of chirality using supported cellular structures. Adv. Mater. 25 (24), 3380–3385. http://dx.doi.org/10.1002/adma.201300617, URL: https://onlinelibrary.wiley.com/doi/abs/10.1002/adma.201300617.

Krause, S., Evans, J.D., Bon, V., Senkovska, I., Iacomi, P., Kolbe, F., Ehrling, S., Troschke, E., Getzschmann, J., Többens, D.M., et al., 2019. Towards general network architecture design criteria for negative gas adsorption transitions in ultraporous frameworks. Nature Commun. 10 (1), 3632.

Le Duigou, A., Chabaud, G., Scarpa, F., Castro, M., 2019. Bioinspired electro-thermo-hygro reversible shape-changing materials by 4D printing. Adv. Funct. Mater. 29 (40), 1903280.

Le Duigou, A., Fruleux, T., Matsuzaki, R., Chabaud, G., Ueda, M., Castro, M., 2021. 4D printing of continuous flax-fibre based shape-changing hygromorph biocomposites: Towards sustainable metamaterials. Mater. Des. 211, 110158.

Lefèvre, V., Danas, K., Lopez-Pamies, O., 2017. A general result for the magnetoelastic response of isotropic suspensions of iron and ferrofluid particles in rubber, with applications to spherical and cylindrical specimens. J. Mech. Phys. Solids 107, 343–364.

Li, Z., Yang, Q., Fang, R., Chen, W., Hao, H., 2021. Origami metamaterial with two-stage programmable compressive strength under quasi-static loading. Int. J. Mech. Sci. 189, 105987. http://dx.doi.org/10.1016/j.ijmecsci.2020.105987, URL: https://www.sciencedirect.com/science/article/pii/S0020740320316945.

Liu, J.A.-C., Gillen, J.H., Mishra, S.R., Evans, B.A., Tracy, J.B., 2019. Photothermally and magnetically controlled reconfiguration of polymer composites for soft robotics. Sci. Adv. 5 (8), eaaw2897. http://dx.doi.org/10.1126/sciadv.aaw2897, URL: https://advances.sciencemag.org/content/5/8/eaaw2897.

Liu, J., Gu, T., Shan, S., Kang, S.H., Weaver, J.C., Bertoldi, K., 2016. Harnessing buckling to design architected materials that exhibit effective negative swelling. Adv. Mater. 28 (31), 6619–6624. http://dx.doi.org/10.1002/adma.201600812, URL: https://onlinelibrary.wiley.com/doi/abs/10.1002/adma.201600812.

Lu, M.-H., Feng, L., Chen, Y.-F., 2009. Phononic crystals and acoustic metamaterials. Mater. Today 12 (12), 34–42. http://dx.doi.org/10.1016/S1369-7021(09)70315-3, URL: http://www.sciencedirect.com/science/article/pii/S1369702109703153.

Maconachie, T., Leary, M., Lozanovski, B., Zhang, X., Qian, M., Faruque, O., Brandt, M., 2019. SLM lattice structures: Properties, performance, applications and challenges. Mater. Des. 183, 108137.

Mao, Y., Wang, W.L., Wei, D., Kaxiras, E., Sodroski, J.G., 2011. Graphene structures at an extreme degree of buckling. ACS Nano 5 (2), 1395–1400.

Mayer, F., Ryklin, D., Wacker, I., Curticean, R., Čalkovsky, M., Niemeyer, A., Dong, Z., Levkin, P.A., Gerthsen, D., Schröder, R.R., et al., 2020. 3D two-photon microprinting of nanoporous architectures. Adv. Mater. 32 (32), 2002044.

McWeeny, R., 2002. Symmetry: an Introduction To Group Theory and Its Applications. Courier Corporation.

Meaud, J., Che, K., 2017. Tuning elastic wave propagation in multistable architected materials. Int. J. Solids Struct. 122–123, 69–80. http://dx.doi.org/10.1016/j.ijsolstr.2017.05.042, URL: https://www.sciencedirect.com/science/article/pii/S0020768317302561.

Miyoshi, H., Matsubara, S., Okumura, D., 2021. Bifurcation and deformation during the evolution of periodic patterns on a gel film bonded to a soft substrate. J. Mech. Phys. Solids 148, 104272.

Mullin, T., Deschanel, S., Bertoldi, K., Boyce, M.C., 2007. Pattern transformation triggered by deformation. Phys. Rev. Lett. 99 (8), 084301. http://dx.doi.org/10.1103/PhysRevLett.99.084301, URL: https://link.aps.org/doi/10.1103/PhysRevLett.99.084301.

Nagy, D.A., 1979. Modal representation of geometrically nonlinear behavior by the finite element method. Comput. Struct. 10 (4), 683–688. http://dx.doi.org/10.1016/0045-7949(79)90012-9, URL: https://www.sciencedirect.com/science/article/pii/0045794979900129.

Neville, R.M., Scarpa, F., Pirrera, A., 2016. Shape morphing Kirigami mechanical metamaterials. Sci. Rep. 6 (1), 31067. http://dx.doi.org/10.1038/srep31067, URL: https://www.nature.com/articles/srep31067.

Nguyen, Q.S., 2000. Stability and Nonlinear Solid Mechanics. Wiley.

Ohno, N., Okumura, D., Noguchi, H., 2002. Microscopic symmetric bifurcation condition of cellular solids based on a homogenization theory of finite deformation. J. Mech. Phys. Solids 50 (5), 1125–1153. http://dx.doi.org/10.1016/S0022-5096(01)00106-5, URL: http://www.sciencedirect.com/science/article/pii/S0022509601001065.

Okumura, D., Ohno, N., Noguchi, H., 2002. Post-buckling analysis of elastic honeycombs subject to in-plane biaxial compression. Int. J. Solids Struct. 39 (13), 3487–3503. http://dx.doi.org/10.1016/S0020-7683(02)00165-8, URL: http://www.sciencedirect.com/science/article/pii/S0020768302001658.

Overvelde, J.T.B., Bertoldi, K., 2014. Relating pore shape to the non-linear response of periodic elastomeric structures. J. Mech. Phys. Solids 64, 351–366. http://dx.doi.org/10.1016/j.jmps.2013.11.014, URL: https://www.sciencedirect.com/science/article/pii/S0022509613002482.

Overvelde, J.T.B., de Jong, T.A., Shevchenko, Y., Becerra, S.A., Whitesides, G.M., Weaver, J.C., Hoberman, C., Bertoldi, K., 2016. A three-dimensional actuated origami-inspired transformable metamaterial with multiple degrees of freedom. Nature Commun. 7 (1), 10929. http://dx.doi.org/10.1038/ncomms10929, URL: https://www.nature.com/articles/ncomms10929.

Overvelde, J.T.B., Shan, S., Bertoldi, K., 2012. Compaction through buckling in 2D periodic, soft and porous structures: effect of pore shape. Adv. Mater. 24 (17), 2337–2342. http://dx.doi.org/10.1002/adma.201104395, URL: https://onlinelibrary.wiley.com/doi/abs/10.1002/adma.201104395.

Overvelde, J.T.B., Weaver, J.C., Hoberman, C., Bertoldi, K., 2017. Rational design of reconfigurable prismatic architected materials. Nature 541 (7637), 347–352. http://dx.doi.org/10.1038/nature20824, URL: https://www.nature.com/articles/nature20824.

Pandurangi, S.S., Akerson, A., Elliott, R.S., Healey, T.J., Triantafyllidis, N., 2022. Nucleation of creases and folds in hyperelastic solids is not a local bifurcation. J. Mech. Phys. Solids 160, 104749.

Papka, S.D., Kyriakides, S., 1994. In-plane compressive response and crushing of honeycomb. J. Mech. Phys. Solids 42 (10), 1499–1532. http://dx.doi.org/10.1016/0022-5096(94)90085-X, URL: http://www.sciencedirect.com/science/article/pii/002250969490085X.

Papka, S.D., Kyriakides, S., 1998. In-plane crushing of a polycarbonate honeycomb. Int. J. Solids Struct. 35 (3), 239–267. http://dx.doi.org/10.1016/S0020-7683(97)00062-0, URL: https://www.sciencedirect.com/science/article/pii/S0020768397000620.

Papka, S.D., Kyriakides, S., 1999a. Biaxial crushing of honeycombs: —Part 1: Experiments. Int. J. Solids Struct. 36 (29), 4367–4396. http://dx.doi.org/10.1016/S0020-7683(98)00224-8, URL: http://www.sciencedirect.com/science/article/pii/S0020768398002248.

Papka, S.D., Kyriakides, S., 1999b. In-plane biaxial crushing of honeycombs—: Part II: Analysis. Int. J. Solids Struct. 36 (29), 4397–4423. http://dx.doi.org/10.1016/S0020-7683(98)00225-X, URL: http://www.sciencedirect.com/science/article/pii/S002076839800225X.

Pennec, Y., Vasseur, J.O., Djafari-Rouhani, B., Dobrzyński, L., Deymier, P.A., 2010. Two-dimensional phononic crystals: Examples and applications. Surf. Sci. Rep. 65 (8), 229–291. http://dx.doi.org/10.1016/j.surfrep.2010.08.002, URL: http://www.sciencedirect.com/science/article/pii/S0167572910000555.

Pishvar, M., Harne, R.L., 2020. Foundations for soft, smart matter by active mechanical metamaterials. Adv. Sci. 7 (18), 2001384. http://dx.doi.org/10.1002/advs.202001384, URL: https://onlinelibrary.wiley.com/doi/abs/10.1002/advs.202001384.

du Plessis, A., Razavi, S.M.J., Benedetti, M., Murchio, S., Leary, M., Watson, M., Bhate, D., Berto, F., 2021. Properties and applications of additively manufactured metallic cellular materials: a review. Prog. Mater. Sci. 100918.

Poncelet, M., Somera, A., Morel, C., Jailin, C., Auffray, N., 2018. An experimental evidence of the failure of Cauchy elasticity for the overall modeling of a non-centro-symmetric lattice under static loading. Int. J. Solids Struct. 147, 223–237. http://dx.doi.org/10.1016/j.ijsolstr.2018.05.028, URL: https://www.sciencedirect.com/science/article/pii/S0020768318302221.

Psarra, E., Bodelot, L., Danas, K., 2017. Two-field surface pattern control via marginally stable magnetorheological elastomers. Soft Matter 13 (37), 6576–6584.

Psarra, E., Bodelot, L., Danas, K., 2019. Wrinkling to crinkling transitions and curvature localization in a magnetoelastic film bonded to a non-magnetic substrate. J. Mech. Phys. Solids 133, 103734.

Qu, J., Kadic, M., Naber, A., Wegener, M., 2017. Micro-structured two-component 3d metamaterials with negative thermal-expansion coefficient from positive constituents. Sci. Rep. 7 (1), 40643. http://dx.doi.org/10.1038/srep40643, URL: https://www.nature.com/articles/srep40643.

Reddy, J.N., 2014. An Introduction To Nonlinear Finite Element Analysis Second Edition: With Applications To Heat Transfer, Fluid Mechanics, and Solid Mechanics. OUP Oxford.

Rouche, N., Habets, P., Laloy, M., 1977. Stability of a mechanical equilibrium. In: Rouche, N., Habets, P., Laloy, M. (Eds.), Stability Theory By Liapunov's Direct Method. In: Applied Mathematical Sciences, Springer, New York, NY, pp. 97–127. http://dx.doi.org/10.1007/978-1-4684-9362-7_3.

Saiki, I., Ikeda, K., Murota, K., 2005. Flower patterns appearing on a honeycomb structure and their bifurcation mechanism. Int. J. Bifurcation Chaos 15 (02), 497–515. http://dx.doi.org/10.1142/S021812740501217X, URL: https://www.worldscientific.com/doi/abs/10.1142/S021812740501217X.

Schaedler, T.A., Carter, W.B., 2016. Architected cellular materials. Annu. Rev. Mater. Res. 46 (1), 187–210. http://dx.doi.org/10.1146/annurev-matsci-070115-031624, URL: http://www.annualreviews.org/doi/10.1146/annurev-matsci-070115-031624.

Shan, S., Kang, S.H., Wang, P., Qu, C., Shian, S., Chen, E.R., Bertoldi, K., 2014. Harnessing multiple folding mechanisms in soft periodic structures for tunable control of elastic waves. Adv. Funct. Mater. 24 (31), 4935–4942. http://dx.doi.org/10.1002/adfm.201400665, URL: https://onlinelibrary.wiley.com/doi/abs/10.1002/adfm.201400665.

Shang, X., Liu, L., Rafsanjani, A., Pasini, D., 2018. Durable bistable auxetics made of rigid solids. J. Mater. Res. 33 (3), 300–308. http://dx.doi.org/10.1557/jmr.2017.417, URL: https://www.cambridge.org/core/journals/journal-of-materials-research/article/abs/durable-bistable-auxetics-made-of-rigid-solids/3B94ACE298618E4F8804F1F891760709.

Shaw, L.A., Hopkins, J.B., 2015. An actively controlled shape-morphing compliant microarchitectured material. J. Mech. Robotics 8 (021019), http://dx.doi.org/10.1115/1.4031168.

Shim, J., Perdigou, C., Chen, E.R., Bertoldi, K., Reis, P.M., 2012. Buckling-induced encapsulation of structured elastic shells under pressure. Proc. Natl. Acad. Sci. 109 (16), 5978–5983.

Shim, J., Wang, P., Bertoldi, K., 2015. Harnessing instability-induced pattern transformation to design tunable phononic crystals. Int. J. Solids Struct. 58, 52–61. http://dx.doi.org/10.1016/j.ijsolstr.2014.12.018, URL: https://www.sciencedirect.com/science/article/pii/S0020768314004880.

Song, Y., Dohm, P.C., Haghpanah, B., Vaziri, A., Hopkins, J.B., 2016. An active microarchitectured material that utilizes piezo actuators to achieve programmable properties. Adv. Eng. Mater. 18 (7), 1113–1117. http://dx.doi.org/10.1002/adem.201500607, URL: https://onlinelibrary.wiley.com/doi/abs/10.1002/adem.201500607.

Song, Z., Wang, X., Lv, C., An, Y., Liang, M., Ma, T., He, D., Zheng, Y.-J., Huang, S.-Q., Yu, H., Jiang, H., 2015. Kirigami-based stretchable lithium-ion batteries. Sci. Rep. 5 (1), 10988. http://dx.doi.org/10.1038/srep10988, URL: https://www.nature.com/articles/srep10988.

Spiegel, C.A., Hippler, M., Münchinger, A., Bastmeyer, M., Barner-Kowollik, C., Wegener, M., Blasco, E., 2020. 4D printing at the microscale. Adv. Funct. Mater. 30 (26), 1907615.

Surjadi, J.U., Gao, L., Du, H., Li, X., Xiong, X., Fang, N.X., Lu, Y., 2019. Mechanical metamaterials and their engineering applications. Adv. Eng. Mater. 21 (3), 1800864. http://dx.doi.org/10.1002/adem.201800864, URL: https://onlinelibrary.wiley.com/doi/abs/10.1002/adem.201800864.

Triantafyllidis, N., Peek, R., 1992. On stability and the worst imperfection shape in solids with nearly simultaneous eigenmodes. Int. J. Solids Struct. 29 (18), 2281–2299. http://dx.doi.org/10.1016/0020-7683(92)90216-G, URL: https://www.sciencedirect.com/science/article/pii/002076839290216G.

Triantafyllidis, N., Schraad, M.W., 1998. Onset of failure in aluminum honeycombs under general in-plane loading. J. Mech. Phys. Solids 46 (6), 1089–1124. http://dx.doi.org/10.1016/S0022-5096(97)00060-4, URL: http://www.sciencedirect.com/science/article/pii/S0022509697000604.

Turcaud, S., Guiducci, L., Fratzl, P., Bréchet, Y.J., Dunlop, J.W., 2011. An excursion into the design space of biomimetic architectured biphasic actuators. Int. J. Mater. Res. 102 (6), 607–612.

Vanderbauwhede, A., 1980. Symmetry and bifurcation near families of solutions. J. Differential Equations 36 (2), 173–187. http://dx.doi.org/10.1016/0022-0396(80)90062-5, URL: https://www.sciencedirect.com/science/article/pii/0022039680900625.

Viard, A.-E., Dirrenberger, J., Forest, S., 2020. Propagating material instabilities in planar architectured materials. Int. J. Solids Struct. 202, 532–551. http://dx.doi.org/10.1016/j.ijsolstr.2020.05.027.

Wang, Z., Bouaziz, O., Dirrenberger, J., Lapouge, P., 2023. Corrugation reinforced architectured materials by direct laser hardening: a study of geometrically induced work hardening in steel. Steel Res. Int. http://dx.doi.org/10.1002/srin.202200695.

Wang, Q., Jackson, J.A., Ge, Q., Hopkins, J.B., Spadaccini, C.M., Fang, N.X., 2016. Lightweight mechanical metamaterials with tunable negative thermal expansion. Phys. Rev. Lett. 117 (17), 175901. http://dx.doi.org/10.1103/PhysRevLett.117.175901, URL: https://link.aps.org/doi/10.1103/PhysRevLett.117.175901.

Waszczyszyn, Z., 1983. Numerical problems of nonlinear stability analysis of elastic structures. Comput. Struct. 17 (1), 13–24. http://dx.doi.org/10.1016/0045-7949(83)90023-8, URL: https://www.sciencedirect.com/science/article/pii/0045794983900238.

Waszczyszyn, Z., Cichon, C., Radwanska, M., 2013. Stability of Structures By Finite Element Methods. Elsevier.

Wei, Y.-L., Yang, Q.-S., Ma, L.-H., Tao, R., Shang, J.-J., 2020. Design and analysis of 2D/3D negative hydration expansion Metamaterial driven by hydrogel. Mater. Des. 196, 109084. http://dx.doi.org/10.1016/j.matdes.2020.109084, URL: https://www.sciencedirect.com/science/article/pii/S0264127520306195.

Wilcox, C.H., 1977. Theory of Bloch Waves. Technical Report, Utah Univ Salt Lake City Dept of Mathematics.

Wriggers, P., 2008. Stability Problems. In: Wriggers, P. (Ed.), Nonlinear Finite Element Methods. Springer, Berlin, Heidelberg, pp. 255–271. http://dx.doi.org/10.1007/978-3-540-71001-1_7.

Xia, X., Afshar, A., Yang, H., Portela, C.M., Kochmann, D.M., Di Leo, C.V., Greer, J.R., 2019. Electrochemically reconfigurable architected materials. Nature 573 (7773), 205–213. http://dx.doi.org/10.1038/s41586-019-1538-z, URL: https://www.nature.com/articles/s41586-019-1538-z.

Yang, Y., Dias, M.A., Holmes, D.P., 2018. Multistable kirigami for tunable architected materials. Phys. Rev. Mater. 2 (11), 110601. http://dx.doi.org/10.1103/PhysRevMaterials.2.110601, URL: https://link.aps.org/doi/10.1103/PhysRevMaterials.2.110601.

Zhang, Q., Yang, X., Li, P., Huang, G., Feng, S., Shen, C., Han, B., Zhang, X., Jin, F., Xu, F., et al., 2015. Bioinspired engineering of honeycomb structure–Using nature to inspire human innovation. Prog. Mater. Sci. 74, 332–400.